Three-dimensional cellularization in chytrid fungi uses distinct mechanisms from those driving one- and two-dimensional cytokinesis in animals and yeast

Edgar M Medina[1], Mary W Elting[2], Lillian Fritz-Laylin[3]

[1]Department of Biology, University of Massachusetts, Amherst, MA, 01003, United States

[2]Cluster for Quantitative and Computational Developmental Biology and the Department of Physics, North Carolina State University, Raleigh, NC, 27695, United States

[3]Howard Hughes Medical Institute and the Department of Biology, University of Massachusetts, Amherst, MA, 01003, United States

ABSTRACT

Chytrid fungi offer a unique opportunity to study three-dimensional cellularization, where nuclei that start out homogeneously distributed throughout the cytoplasm are synchronously compartmentalized into daughter cells. This process addresses geometric challenges not encountered in conventional cytokinesis, where nuclei are organized in a one-dimensional line, or in *Drosophila* cellularization, which is organized in a two-dimensional plane—both of which allow nuclei direct access to cytokinetic cues placed at the plasma membrane. Here, we show that three-dimensional cellularization in the chytrid *Spizellomyces punctatus* proceeds through a stepwise program, beginning with the transient migration of nuclei and their associated centrosomes to the plasma membrane. At this point, centrosome-associated vesicles form and initiate membrane invagination, establishing tubular furrows that expand and branch, ultimately creating a foam-like tessellation of tightly packed polyhedral compartments, each containing a single nucleus and bearing a cilium. Using a combination of small molecule inhibitors and laser ablation, we demonstrate that, similar to cytokinesis and *Drosophila* cellularization, chytrid cellularization is powered by actomyosin networks. We also show that while microtubules are important for patterning, they appear dispensable for cellularization. Finally, we suggest that chytrids may have incorporated mechanisms associated with ciliogenesis in animals to coordinate the association of internal nuclei with actomyosin networks and membranes. These data highlight the value of using chytrid fungi to study the unique geometric problems associated with three-dimensional cellularization.

INTRODUCTION

Animal and fungal cells divide by forming a trench-like membrane furrow that separates daughter nuclei into two distinct compartments (Glotzer, 2017; Pollard and O'Shaughnessy, 2019). This type of cytokinesis usually occurs immediately after nuclear division with the two daughter nuclei arranged in a straight line.. However, when multiple rounds of nuclear division occur before cytokinesis, the resulting multinuclear cell state must be resolved by more complex

cellularization processes. During *Drosophila* development, for example, hundreds of nuclei arrange themselves in a uniform monolayer near the plasma membrane, making the outcome of cellularization a two-dimensional sheet of cells at the surface of the blastoderm (Sokac et al., 2023). Chytrid fungi represent an even more complex example that takes the geometry of cellularization to the third dimension. These deep evolutionary lineages of fungi reproduce by compartmentalizing dozens of nuclei that are distributed homogeneously throughout the cytoplasm, resulting in a ball—or morula—of uninucleated daughter cells of uniform volume, each bearing a motile cilium. The mechanisms that organize and drive this three-dimensional form of cellularization remain unclear.

Despite having different geometries, one-dimensional, and two-dimensional cellularization involves four fundamental steps. First, nuclei find their positions. Second, the division site is selected. Third, the cell builds a cleavage structure at the division site. Fourth, the cleavage structure separates the mother cell into daughter cells. Animal and yeast cells use the same general strategies to complete these four steps. Both lineages rely on the pushing and pulling forces of microtubules to position their nuclei (Deshpande and Telley, 2021; Padilla et al., 2022; Xiang, 2018). Both use plasma membrane-anchored cues to define the position of the cleavage furrow (Glotzer, 2017; Pollard and O'Shaughnessy, 2019). Finally, both drive centripetal (inward) ingression of a trench-like furrow using a contractile ring made of actin and myosin-II (Glotzer, 2017; Pollard and O'Shaughnessy, 2019). Despite their widespread use across animals, yeasts, and slime molds, these basic strategies cannot be extrapolated directly to three-dimensional cellularization for two reasons. First, interior nuclei are obstructed from access to cues placed on the plasma membrane. Second, it is not obvious how the contraction of actomyosin rings assembled at the plasma membrane during one- and two-dimensional cellularization could generate the many planes needed to surround the inner nuclei present during three-dimensional cytokinesis. Thus, it remains unclear whether and how the mechanisms used for conventional cytokinesis and two-dimensional cellularization apply to three-dimensional chytrid cellularization.

Here, we dissect the molecular mechanisms driving three-dimensional cellularization in the chytrid fungus *Spizellomyces punctatus*. We identify the main stages of cellularization and use pharmacological and physical perturbations to disrupt them. We find that the molecular mechanisms driving chytrid cellularization involve a combination of actomyosin machinery similar to that used for conventional cytokinesis along with ciliogenesis-like events. One-, two-, and three-dimensional cellularization therefore together represent a key example of different cellular events that use the same molecular machinery for the same objective via distinct molecular mechanisms.

RESULTS

Membranes colocalize with actin and myosin-II activity to form a 3-dimensional cellularization lattice.

To begin, we confirmed that cellularization is indeed 3-dimensional in *Spizellomyces punctatus* (*Sp*). To determine the spatial distribution of nuclei and membrane during peak cellularization—the stage in which the network of cellularization furrows occupies the full cytoplasm of the mother cell—we developed a method to grow synchronized cultures of *Sp* adhered to glass imaging dishes (see methods). With this system, we tracked nuclei using a native nuclear localization signal fused to the fluorescent protein mClover3 as well as membranes using the fluorescent dye FM4-64. Using 3D point-scanner confocal imaging, we found that during peak cellularization, each nucleus is enveloped inside a polyhedron-shaped

membrane (**Figure 1A**). These uninucleated polyhedra are tightly packed throughout the spherical sporangium—like soap bubbles inside a container—confirming that chytrid cellularization is indeed three-dimensional.

To determine how the cellularization lattice forms, we conducted time-lapse microscopy of FM4-64-stained membranes during cellularization and identified five main stages of membrane reorganization (**Figure 1B & C**). First, small, spherical invaginations form at the plasma membrane **(Stage 1)**. These "furrow initials" extend and elongate inwards toward the center of the cell, forming a membrane projection similar to a tubule, tunnel, or well that we call a "furrow" **(Stage 2)**. These furrows then invade the cytoplasm, branching and merging as they grow **(Stage 3)**, resulting in a tightly packed polyhedral network that occupies the entire sporangium **(Stage 4)**. Finally, in a single synchronous event called abscission, all of the polyhedra turn into spheres and separate from each other to form daughter cells. The resulting individual cells then swim and/or crawl out of one or more discharge pores in the sporangial cell wall, leaving behind the empty shell of their mother **(Stage 5)**.

To dissect in more detail the geometric patterning formed during chytrid cellularization, we measured the angles formed at the vertices of the cellularization polyhedra (**Figure 1D**) and the distribution of daughter zoospores generated via cellularization (**Figure 1E**). We found that the vertices show three furrows meeting on average at 120 degrees. This is consistent with zoospore territories of hexagonal symmetry. We also found that chytrid cellularization produces daughter zoospores of very homogenous size, of about 2.89 micrometers, with 95% of cells within only 0.57 microns from the mean size which is only 60% worse than artificial latex beads of 2 microns (**Figure 1E**). Together, these results show that the mechanisms of chytrid cellularization must produce a tessellation of polyhedra of primarily hexagonal symmetry of very homogenous volume.

We next identified cellular machinery associated with the formation of the cellularization polyhedra. Animal and yeast cellularization relies on conserved cytoskeletal elements, primarily actin, myosin-II, and microtubules (Pollard and O'Shaughnessy, 2019). To explore the roles of these elements in chytrid cellularization, we visualized the distribution of actin networks with the actin polymer-binding probe Lifeact fused to the fluorescent protein mClover3 and co-staining cells with FM4-64. We found that during peak cellularization, actin, and membrane colocalize to the polyhedral cellularization lattice (**Figure 1F**). We also determined the distribution of a fluorescently-tagged myosin regulatory light chain (MRLC)—a proxy for myosin-II activity (Heissler and Sellers, 2015). We found that, like actin, the fluorescent MRLC colocalizes with the membrane in the cellularization lattice, suggesting a possible role of contractile actomyosin in chytrid cellularization (**Figure 1F**). Finally, by expressing a fluorescently tagged α-tubulin, we observed two structures closely associated with each nucleus during peak cellularization: a cilium as well as a centriolar microtubule organizing center and associated astral microtubules that extend from the centrosome toward the cell cortex (**Figure 1F**). Together, these results show that cellularization in chytrids may rely on similar cytoskeletal elements as the cellularization of animal and yeast cells.

These results show that the assembly of the cellularization lattice in chytrids is initiated at the plasma membrane, much like in yeast or animal cells. However, unlike animals and yeast, chytrids do not use typical trench-like furrows. Instead, chytrid furrows form as individual vesicles in the plasma membrane that extend into independent tubular "wells" that invade, merge, and weave together to form a tessellation of membrane polyhedra of homogenous volume and hexagonal symmetry.

Nuclear migration to the plasma membrane precedes the onset of cellularization.

In animal and yeast cytokinesis, as well as during *Drosophila* 2D cellularization, daughter nuclei remain stationary while cytokinetic furrows extend between or around them. Because nuclei remain highly dynamic during chytrid cellularization, it is unclear if nuclear position plays a role in defining the position, number, and assembly of furrows. To explore possible coordination between nuclear movement and furrow formation, we imaged synchronized cultures marked for membranes with FM4-64 and nuclei with a fluorescently tagged histone H2B. Imaging cross-sections through the center of sporangia revealed a possible enrichment of nuclei at the cell surface just before cellularization (**Figure 2A**). To quantify this observation, we calculated the ratio of nuclei in two regions of equivalent area: an outer donut at the surface of the sporangium and the remaining inner disk—the cortical nuclear ratio. This ratio was near one before and during cellularization, except for a short window of ten minutes in which nuclei are enriched in the cortical region (**Figure 2A-B**) that coincides with furrow initiation (Stage 1) and elongation (Stage 2). The maximal nuclear enrichment is closely associated with the start of furrow elongation (Stage 2), with 92% (22 out of 24) of sporangia progressing into furrow elongation (Stage 2) within five minutes of the peak nuclear cortical ratio (**Figure 2B; Supplementary Figure S1**). Thus, entry into cellularization is marked by the recruitment of nuclei to the plasma membrane.

To further explore the relationship between nuclear position and furrow initiation, we imaged at a higher frame rate and found that vesicular furrow initials form in proximity to the nuclei at the plasma membrane (**Figure 2C**). Imaging of the nuclei approaching entry into cellularization showed a progressive formation of vesicular furrow initials near cortical nuclei (**Figure 2C**). Because animal cells use astral microtubules to position furrows (Pollard and O'Shaughnessy, 2019), we hypothesized that patterning of chytrid cellularization may also involve microtubules. To test this hypothesis we followed cellularization in a strain expressing fluorescent tubulin (mClover3-alpha-Tubulin) in the presence of FM4-64 (**Figure 3A & B**). We found that each nucleus in an actively growing sporangium is associated with two opposing foci of tubulin fluorescence. Because these foci turn into spindle poles and duplicate immediately after nuclear division (**Supplementary Figure S2**), we infer that these foci are centriolar centrosomes. Consistent with these microtubule organizing centers playing a role in furrow positioning, we observed furrow initials forming in between the centrosomes and the plasma membrane (**Figure 3A & B**). To confirm that the furrows form near the centrosomes, we built a strain expressing a fluorescently tagged version of SAS-6, a core component of eukaryotic centrioles (Leidel et al., 2005). Cells expressing fluorescent SAS-6 show fluorescent foci at spindle poles and the base of the ciliary axoneme consistent with a centriolar distribution of SAS-6-mClover3. Upon entry into cellularization, SAS-6 puncta approach the plasma membrane, where they become associated with the furrow initials highlighted by FM4-64 (**Figure 3C**). These results show that during entry into cellularization, nuclei along with their associated centrosomes are transiently recruited to the plasma membrane, where they mark the site—and may trigger the formation—of the vesicular furrow initials.

To further understand the relationship between furrow formation and nuclear positioning, we followed the position of nuclei, centrosomes, and membrane through the later stages of cellularization. Consistent with centrosomes playing a major role in organizing chytrid cellularization, we found that during furrow elongation (Stage 2) the centrosomes appear to remain tethered to the leading front of the furrow initials, dragging their nucleus with it. This behavior suggests that centrosomes may dock to the vesicular furrows, thereby tethering nuclei to the furrows during cellularization.

Microtubules are important for geometric patterning but are not necessary for cellularization.

Forces transmitted through microtubules help move and position the nuclei or the spindle during cytokinesis in animal and yeast systems (Burgess and Chang, 2005; Daga and Chang, 2005; Harvey, 1935; Rappaport, 1996, 1986). During *Drosophila* 2D cellularization, for example, microtubules move and position the nuclei in a monolayer under the plasma membrane in preparation for cellularization (Baker et al., 1993; Deshpande et al., 2022; Sokac et al., 2023). Furthermore, plus-directed motors that ride on microtubules (Kinesin-6; Pav-KLP) may provide the driving force required during the early stages of furrow ingression and deliver via vesicles the actin and membrane required during *Drosophila* 2D cellularization (Minestrini et al., 2003; Sokac et al., 2023; Sommi et al., 2010). We therefore wondered if the microtubules nucleated from chytrid centrosomes play a similar role in furrow elongation. To test this hypothesis, we depolymerized the microtubules of cellularizing sporangia using 2uM Nocodazole in a chytrid strain expressing fluorescent tubulin. Unlike cells treated with DMSO alone as a carrier control, sporangia treated with Nocodazole showed rapid dissipation of all microtubule structures except for a bright dot at the centrosome (**Supplementary Figure S3**). These cells formed cellularization polyhedra of uneven size with curved edges and rounded vertices **(Figure 4A)**. Despite these patterning defects, Nocodazole-treated sporangia completed cellularization, producing daughter cells that lacked cilia (**Supplementary Figure S3**). In contrast, sporangia treated with DMSO alone assembled well-organized cellularization lattices **(Figure 4A)** and produced normal, ciliated daughter cells.

To quantify the patterning defect induced by microtubule depolymerization, we compared the size and variance of the cellularization polyhedra between nocodazole-treated and control cells. To aid automated image analysis, we focused on the polyhedra contiguous to the sporangial cell wall because they have regular, perpendicular furrows (**Figure 3A**). We found that, while sporangia treated with DMSO produced polyhedra with diameters between 3-3.5 microns, sporangia treated with Nocodazole produced polyhedra between 2.5-3 microns—a 14% reduction in diameter, and an even greater change in its variance (**Figure 3B**). These results show that, while microtubules are not strictly necessary for chytrid cellularization, they are key players in defining the pattern and spacing of the cellularization polyhedra.

The additional membrane needed for cellularization is sourced from the Golgi.

Building the three-dimensional cellularization lattice requires large amounts of membrane. Since the membrane used for cytokinesis in animals and yeasts comes from the Golgi, we wondered if this was also the case for chytrid cellularization. To test this hypothesis, we disrupted ER-to-Golgi trafficking with the drug Brefeldin A (BFA) (**Figure 3 C, D, & E**). We treated synchronous populations of *Sp* with either 50uM BFA—or DMSO carrier control—in the presence of FM4-64 and followed sporangial development by time-lapse imaging for six hours (**Figure 3 C & D)**. To facilitate visualization of the cellularization pattern, we performed “unwrapping” of the circular sporangia by polar transformation (**Figure 3 C)**. While control sporangia completed cellularization within the imaging window (N=127), only 7% of sporangia treated with BFA completed cellularization (N=206),12 out of 14 of which had already started cellularization when BFA was added **(Figure 3 E)**. The sporangia that failed to cellularize displayed two main phenotypes. The first was “failure to start”. Sporangia with this phenotype were in either Stage 1 (pre-cellularization) or Stage 2 (with some level of furrow branching) **(Figure 3 D)**. Although the furrows of these cells made repeated movements toward the cell

interior, these sporangia never progressed further in cellularization and eventually arrested cytoplasmic movement, vesiculated, and acquired intense, uniform FM4-64 fluorescence—suggestive of cell death. The second phenotype was “network collapse”, which occurred in sporangia that already had an advanced cellularization network (Stage 3) before BFA treatment (**Figure 3D**). The cellularization structures in these cells collapse into a single disorganized bundle and then gradually disappear until the cell appears to die in the same way as the “failure to start” phenotype. Together, these results show that active ER-to-Golgi trafficking is necessary for the formation and maintenance of the chytrid cellularization network and that the membrane for cellularization is likely to be sourced primarily from the Golgi.

Actomyosin is a driving force of chytrid 3D cellularization.

Having shown that microtubules are not necessary for chytrid cellularization, we next asked whether cellularization requires dynamic actin structures. Therefore, we treated cellularizing sporangia expressing a fluorescently-tagged F-actin probe (Lifeact) with Latrunculin B (LatB)—a reversible inhibitor of actin polymerization that sequesters actin monomers and prevents their incorporation into actin filaments and accelerates depolymerization(Coué et al., 1987; Fujiwara et al., 2018). Treatment with LatB caused a complete disassembly of cellularization networks within five minutes (**Figure 5 A**). This effect was reversible, as the cellularization networks began reforming within five minutes of washing out LatB. We quantified these phenotypes using fluorescence intensity variability (i.e. Haralick image texture) as a proxy for the structural complexity of the actin networks (**Figure 5B**). Sporangia treated with DMSO alone showed no significant change in texture. In contrast, sporangia treated with LatB showed a 50-75% increase in homogeneity within five minutes of treatment. Washout of LatB returned texture levels to pre-LatB levels within five minutes. Because Latrunculin B inhibits new F-actin assembly, these results indicate that cellularization networks require active actin polymerization.

In animals and yeast, similar-looking actin networks collaborate with myosin-II motors to generate the contractile forces that drive cytokinesis. To test if myosin-II is also necessary for chytrid cellularization, we treated cellularizing sporangia expressing Lifeact with the myosin-II inhibitor para-amino-blebbistatin (blebbistatin). While sporangia treated with the carrier control DMSO underwent normal cellularization, sporangia treated with blebbistatin failed to complete cellularization (**Figure 5C & D**). These results show that both actin polymerization and myosin-II activity are required for chytrid cellularization.

The actin networks that drive cellularization in animals and yeast rely on myosin-II activity to generate tension. The contractile properties of these networks are commonly tested using pulsed lasers to ablate actomyosin structures in a diffraction-limited spot and observe their movements (Kassianidou et al., 2017; Kumar et al., 2006; Moshtohry et al., 2022; Silva et al., 2016; Spira et al., 2017; Wollrab et al., 2016). If chytrid cellularization is powered by a similar contractile mechanism, then severing the actin furrows should cause the resulting free ends to recoil as they release tension (Moshtohry et al., 2022; Silva et al., 2016; Spira et al., 2017; Wollrab et al., 2016). We therefore used laser ablation to test if the actin networks of both early cellularization furrows and late cellularization polyhedra are under tension.

We first tested whether the actin networks assembled during early cellularization are under tension (Stage 3). Ablation of early cellularization furrows caused large recoils of the actin structures (**Figure 6A**), with the extent and direction of tip recoil varying within and between sporangia. We also observed a tendency of the ablated structures to contract back into the ablated area, as if trying to repair the damaged region (**Figure 6A** kymographs), a reaction

consistent with the response to ablation in other contractile actin networks (Moshtohry et al., 2022; Silva et al., 2016; Spira et al., 2017; Wollrab et al., 2016). To quantify these changes in the speed and direction of the recoil, we used particle image velocimetry (PIV) (**Figure 6B**) using the pixels from the actin network images as tracer particles. After laser ablation, the actin structures near cellularization furrows quickly move away from the ablation point (**Figure 6B**). To measure the speed of these movements, we retrieved the top 10% velocity vectors per PIV frame (one PIV frame being the comparison between consecutive frames separated by one second in the original time-lapse) across the whole sporangium as a proxy for the most dynamic actin networks. This analysis revealed that laser ablation causes a sharp spike in F-actin network velocity that returns to pre-ablation rates within two seconds of ablation (**Figure 6C**). Because the peak velocities map to the ablated region in the vector map (**Figure 6B**), we infer that this increase in velocity corresponds to the recoil of the targeted furrow. These results show that the actomyosin structures weaving the cellularization network are contractile and are under tension.

Finally, we tested whether the F-actin polyhedra of late cellularization are also under tension. We found that laser ablation of the edges of the cellularization polyhedra resulted in a rapid recoil of the furrow tips away from the ablation site (**Figure 6D**). After this first recoil, the two vertices at each side of the ablated furrow also recoiled away from each other causing a dilation in adjacent polyhedra. The tips of the ablated furrow showed a displacement of approximately two micrometers within the first second after ablation, followed by a shallow exponential recoil profile in which tension appear to release for more than 30 seconds (**Figure 6E**). This suggests that most of the tension is released quickly, followed by dilation of the adjacent polyhedra. Together, these results show that contractile actomyosin structures are used during furrow elongation as well as throughout the assembly of the cellularization polyhedra. Furthermore, F-actin network tension is important for establishing and maintaining the geometry of the cellularization network.

DISCUSSION

Here, we dissect the process of chytrid cellularization into molecularly distinct stages (**Figure 7**). Cellularization onset is marked by the migration of nuclei and their associated, outward-facing centrosomes to the plasma membrane, followed by the formation of a vesicle at the point where the centrosome abuts the plasma membrane. These membrane structures project inward in an actomyosin-dependent process, turning into tubular “furrows” that drag the membrane-attached nuclei into the cytoplasm. These tubular furrows expand using membrane sourced from the Golgi. The furrows branch and merge, and eventually settle into a tessellation of tightly-packed polyhedra of homogenous volume each containing a single nucleus. Finally, the polyhedra synchronously separate from each other to form daughter cells that crawl or swim away through a hole in the cell wall of the mother. During cellularization, a centriole associated with each nucleus transitions into a basal body and grows a cilium. We show that, although chytrid cellularization requires actomyosin networks, it uses them in ways that are drastically different from those of animals and yeast.

Chytrids use actomyosin for cellularization but with different mechanisms from animal and yeast cytokinesis.

Chytrids use actomyosin in unique ways to drive three-dimensional cellularization, a process distinct from the actomyosin-driven one-dimensional cellularization (conventional cytokinesis) of

yeast and animal cells and two-dimensional cellularization in *Drosophila*. These one- and two-dimensional processes rely on the assembly of a ring at the plasma membrane that constricts and deforms the membrane into a trench-like furrow around each nucleus. Similarly, chytrids use actomyosin networks to drive membrane invagination during 3D cellularization. However, chytrid cellularization requires building furrows in regions of the cell that do not have ready access to the plasma membrane. Instead of building a furrow around each of the internal nuclei, chytrids recruit nuclei to the plasma membrane prior to furrow initiation and tether each nucleus to a furrow so they remain together while the nuclei are moved inward. Then tubular furrows are used to build the cellularization tessellation. This strategy neatly solves a problem not faced by animal or yeast model systems.

Actomyosin-based multinuclear cellularization is not limited to chytrid fungi and *Drosophila*. The Ichtyosporeans *Sphaeroforma arctica* and *Creolimax fragrantissima* are unicellular relatives of animals that, like *Drosophila*, undergo two-dimensional multinuclear cellularization (Dudin et al., 2019; Suga and Ruiz-Trillo, 2013). The plasmodium of the acellular slime mold *Physarum polycephalum* also likely uses actomyosin for multinuclear cellularization (Goodman and Rusch, 1970; Okamura et al., 1983). Moreover, based on transitions from multinucleate to uninucleate cell states, multinuclear cellularization may also occur during the development and/or germination of slime mold sporocarps, structures that were likely present in the ancestor of the Amoebozoa (Kang et al., 2017). Because the shared ancestor of animals, fungi, and slime molds likely had a multinucleated stage (Skejo et al., 2021), their shared ancestor may have had the capacity to generate uninucleated propagules or gametes through multinuclear cellularization. Here we show that, like animals and Ichtyosporeans, chytrid fungi rely on actomyosin networks to drive multinuclear cellularization, suggesting that this molecular mechanism may also be an ancestral feature of animals and fungi.

Chytrid cellularization combines ciliogenesis and cytokinetic mechanisms in a single cellularization program.

We have shown that chytrids solve the problem of surrounding non-peripheral nuclei with cleavage membranes by moving internal nuclei to the plasma membrane before redistributing them to the cytoplasm. This mechanism comprises three steps: recruitment of the centriole-nuclei to the membrane, the formation of vesicular furrows near each nuclear centrosome, and the tethering of the nuclei to these furrows via the centrosome. These activities resemble key stages of animal ciliogenesis. Ciliogenesis in animal cells starts with the migration of the centriole to the plasma membrane. During this migration, the distal end of one centriole recruits membrane to form a double-membrane sheet called the “ciliary vesicle”. This centriole then docks onto this ciliary vesicle to become a basal body and eventually assembles a ciliary axoneme that emerges from the cell (Zhao et al., 2023).

The morphological similarities between chytrid cellularization and animal ciliogenesis are remarkable. Chytrid vesicular furrow initials resemble animal ciliary vesicles in their vesicular appearance, in how they are formed near cortically migrating centrioles, and in how centrioles appear to dock into them. Ultrastructural studies of chytrid ciliogenesis show a similar “vesicular”-like structure at internal basal bodies called a “primary flagellar vesicle” similar to the animal “ciliary vesicle” (Barron and Hill, 1974; Lessie and Lovett, 1968; Lowry and Roberson, 1997; Renaud and Swift, 1964). Upon recruitment to the plasma membrane, the chytrid nuclei interact with the vesicular furrow initials via the centrosomal region. This attachment persists throughout the rest of cellularization, indicating that nuclear tethering to the cellularization furrows via the centrosome may be equivalent to the centriolar docking in animal ciliogenesis. In

animals, centriolar docking relies on distal appendages and genes associated with human ciliopathies (Tanos et al., 2013). Although many of these genes are also present in chytrids, we do not yet know if and how they are used during cellularization and or ciliogenesis.

The molecular-level similarities between animal intracellular ciliogenesis and early chytrid cellularization are also remarkable. We found that Nocodazole treatment did not inhibit cellularization but did inhibit axonemal elongation. This is similar to ciliogenesis in the quail oviduct, where Nocodazole treatment did not inhibit centrosome migration or centriolar docking but did inhibit axoneme elongation (Boisvieux-Ulrich et al., 1989, 1987). This is in contrast with actin network perturbation, which disrupts both chytrid cellularization and centriolar migration in the quail oviduct (Boisvieux-Ulrich et al., 1990). Thus, chytrids may use animal-like ciliogenetic mechanisms to recruit the centrosomes and their nuclei to the plasma membrane. Because mechanistic details of centrosomal migration during animal ciliogenesis remain unclear (Hannaford and Rusan, 2024), the mechanisms of cortical nuclear migration in chytrids may shed light on centrosomal migration in animal ciliogenesis.

Using chytrids to explore the physics and geometry of foams in biological systems.

We have shown that chytrids cellularize by building a tessellation of polyhedra. We found that, although mother cells vary in size and number of nuclei, the daughter zoospores they produce are remarkably uniform in size. Daughter cell size is directly linked to the geometry of the polyhedra in the tesselation; polyhedra of homogenous volume give rise to daughters of homogenous volume. So how is the pattern, size, and symmetry of the tessellation of polyhedra generated? A hint may come from its similarity to a system of packed soap bubbles, or “foam”. A foam is a collection of surfaces that meet according to Joseph Plateau’s Laws (1873) which state that thin soap films organize in a geometry that minimizes surface area for a given volume (Delsaulx, 1884; Plateau, 1873). More than 100 years ago, the mathematician and natural philosopher D’Arcy Thompson suggested that cellular partitions, tissues, and multicellular aggregates tend to follow the geometrical configurations of soap bubbles to minimize surface area (Thompson, 1945). Since then, the soap bubble analogy has been invoked to explain foam-like patterns in biological systems that arise through distinct mechanisms, such as extracellular force transmission across tissues, differential adhesion between cells, or space-constrained cell division (Agarwal and Zaidel-Bar, 2019; Hayashi and Carthew, 2004; Heer and Martin, 2017; Lecuit and Lenne, 2007). These processes start from separate individual bubbles that interact to eventually give rise to the foam. Although chytrid cellularization resembles these types of foams, the tesselations in this system do not begin with the formation of individual, separate bubbles. Instead, chytrids go straight to building a polyhedral foam wherein all interfacing surfaces and individual polyhedra are built *de novo*.

Generating zoospores is energetically expensive, and evolution may have selected for the most efficient way to compartmentalize a chytrid sporangium into zoospores of defined volume. Under this model, chytrids have evolved to solve a special case of Plateau’s problem called *Kelvin’s Problem*—finding the most efficient "tessellation of space into cells of equal volume with the least surface area" (Thompson, 1887). Kelvin’s problem must be solved by all biological systems that involve complete cellularization within a constrained volume. Therefore, understanding the mechanisms used by chytrids to solve Kelvin’s problem can shed light on the principles of cellular morphogenesis across eukaryotic lineages, as well as inspire new strategies for solving geometrical problems within or without biological systems (Lecuit and Lenne, 2007).

Applying the soap bubble analogy to chytrid cellularization can also help us think about how chytrid mothers produce homogenous daughter cells. Plateau's laws state that: 1) the "bubbles" in the system should have smooth, unbroken surfaces, 2) all points on the same soap film surface have a constant mean curvature, 3) when soap bubble surfaces meet in threes they do so at an angle of 120 degrees—resulting in hexagonal symmetry—and 4) when they meet in fours they do so at an angle of 109.47—tetrahedral symmetry. Our observation of continuous and smooth cleavage membranes that when meeting in three form angles on average of hexagonal symmetry suggest that chytrid cellularization likely obeys at least the first three of these laws. If we assume that chytrid cellularization follows Plateau's Laws, then chytrids cellularize under three spatial constraints: the mother's cell volume is fixed, all compartments have the same "target" volume, and each compartment must contain a single nucleus. This raises important questions regarding the molecular mechanisms underlying how the target cell volume is defined and how the mother builds a compartment around each nucleus. Our results show that microtubule depolymerization results in patterning defects during chytrid cellularization similar to disruptions in nuclear spacing upon microtubule disruption in the distantly related zoosporic fungus *Allomyces* (Lowry and Roberson, 1997). Thus microtubules may help define proper nuclear spacing and a "minimal zoospore territory"—or "target volume"—during chytrid cellularization. Additionally, the tethering of nuclei to the cellularization furrows may help the mother cell keep track of all of the nuclei and serve as guides around which to build each polyhedron.

Concluding remarks.

Chytrid cellularization solves three-dimensional problems that neither animal nor yeast model systems face. Accordingly, we have found that chytrids fulfill each of the four fundamental steps of cellularization using mechanisms that consistently deviate from the general strategies deployed by animal and yeast model systems. First, in animal and yeast cytokinesis, nuclei find and hold their position while cleavage furrows move around them while chytrid nuclei are highly dynamic throughout cellularization. Second, animal and yeast systems rely on plasma membrane-associated cues to recruit and assemble the cytokinetic machinery. While conceptually simple for 1D and 2D cellularization, this constraint is problematic for 3D cellularization because most nuclei lie deep in the cytoplasm, surrounded by other nuclei, and are therefore spatially separated from plasma-membrane bound cues. We found that chytrids solve this problem by recruiting and attaching the nuclei to the plasma membrane, and *then* using actomyosin to build cleavage structures away from the plasma membrane. Third, while animal and yeast cells use trench-like furrows comprising membranes and actomyosin networks as cleavage structures, chytrids use tubular furrows of membranes and actomyosin that only later assemble into a polyhedron around each nucleus. How the tubular structures of early cellularization become polyhedra and how these polyhedra separate into daughter cells remain open questions. Finally, we found that chytrid cellularization may have co-opted ciliogenesis programs, raising the question of whether the similarity between these forms of cell division reflects analogy or homology at the molecular level. Taken together, we have found that chytrids use conserved actomyosin machinery for three-dimensional cellularization but with different mechanisms from those of model system one- and two-dimensional cellularization—a clear reminder that conservation of machinery does not always mean conservation of mechanism.

MATERIALS AND METHODS

Reporter construct design, strain generation, and molecular cloning.

Constructs expressing Lifeact-mClover3v(EM112C: *H2Apr-Lifeact-mClover3-H2Ater :H2Bpr–P2A-T2A-hph-Synther8*), Myosin light regulatory chain (MLRC) (SPPG_07268) fused to mClover3 (pEM100: *SpunMLRCpr-SpunMLRC-mClover3-SpunMLRCter :H2Bpr–P2A-T2A-hph-Synther8*), *Batrachochytrium dendrobatidis* alpha-Tubulin BDEG_00078 fused to mClover3 (EM102: *Bd_aTubpr-mClover3-BdaTub-Bd_aTubter :H2Bpr–P2A-T2A-hph-Synther8*) were synthesized by Twist Bioscience (South San Francisco, United States) and cloned by Twist directly into the binary *Agrobacterium* plasmid pCAMBIA1300 (Addgene: 44183). Plasmids were transformed into *Spizellomyces* and transformant strains were recovered as described previously (Medina et al., 2020; Prostak et al., 2023). *Synther8* is a short synthetic terminator (No 8) from (Curran et al., 2015). Nuclear-localized mClover3 (GI3EM48; *H2Bpr-RbNLS-mClover3-ScADH1ter:H2Apr-hph-ScADH1ter*) was generated using previously published pGI3EM22C (*H2Bpr-Lifeact-tdTomato-ScADH1ter:H2Apr-hph-ScADH1ter*) (Medina et al., 2020) with Lifeact-tdTomato replaced by mClover3 with an N-terminal nuclear localization signal from *Spizellomyces* Rb protein SPPG_07796. Nuclear dynamics from Figure 2 were done with a strain carrying H2B-tdTomato from plasmid pGI3EM20C as previously described (Medina et al., 2020). We sequence-verified all constructs by whole-plasmid sequencing (Plasmidsaurus Inc.). For information about each plasmid used in this study, see **Dataset S1**. Complete plasmid sequences and plasmids have also been deposited at Addgene (***link here***).

Preparation of semi-synchronized cultures for live cell imaging.

Two days prior to the experiment, use DS solution to harvest zoospores from an active culture of *Spizellomyces punctatus* (Koch type isolate NG-3) Barr (ATCC 48900) growing in K1 plates (50mg/L Carbenicillin and tetracycline) with or without selection (200mg/L Hygromycin) as done previously (Medina et al., 2020) and filter zoospores through sterile 40-micron mesh filter (fisherbrand Cat. No. 22363547) followed by a sterile Whatman No1 syringe filter (~11 micron). Plate 1mL of 1/5-1/10 dilution in DS solution of the zoospores into new K1 plates (right out of the fridge), seal with parafilm, and incubate for ~20-24h at 28 Celsius until peak zoospore release—zoospores are ready for seeding the imaging plates.

To prepare the imagining plates, a cellvis 6-well glass bottom black plate with lid (P06-1.5H-N) is cleaned with a plasma cleaner for four minutes at maximum level (Harrick Plasma Expanded Plasma Cleaner 115V). Add promptly 1mL per well of 25ug/mL filter-sterilized 50% w/v polyethyleneimine (PEI) (sigma-Aldrich P3143-100ML) and incubate at room temperature for 10 min. After the 10 min, remove the PEI solution and rinse 10 times with 2mL of sterile DS solution, then add 2mL of sterile DS in preparation for inoculation. Do not let the treated surface dry out. Proceed to prepare the zoospore inoculum.

To seed the imaging plate, harvest and filter the zoospores from the semi-synchronous plate culture made the day before using the same approach as above. Quantify zoospore concentration with a hemocytometer by counting 10uL from a 30uL 1:10 zoospore dilution including 3uL of Lugol solution (Sigma-Aldrich; 62650-100ML-F) (killing zoospores and increasing contrast). Dilute the zoospores with sterile DS to achieve a working stock of 1x10^6 zoospores per mL. Add 1mL of 1x10^6 zoospores per mL of zoospore solution to each well and

leave for 10 min without moving at room temperature. After 10 minutes, tilt and remove the excess zoospore solution and replace it with 2mL of pre-warmed 28C K1 liquid media (50mg/mL carbenicillin; Fisher AAJ6194906), place on top of a 28C pre-warmed aluminum heatblock (two small tube heatblocks taped together) and leave for 10 min. After 10 min, wash gently three times with 2mL of liquid K1 (50mg/mL carbenicillin), then fill with 3mL of liquid K1 (50mg/mL carbenicillin), seal the plate with parafilm and incubate inside a closed plastic container with a humidity chamber (empty pipette tip box with perforated tip rack filled with 50mL water). Incubate for ~18h, at which point they are ready to start cellularization.

Live cell microscopy and laser ablation.

For live cell imaging, cells were imaged on a Nikon Ti2 microscope equipped with a Crest X-Light V2 L-FOV spinning disk (50 µm pinhole), a Prime95B sCMOS camera (Photometrics), and a Plan Apo λ 100x 1.45 NA oil objective, and an Okolab stage top chamber (H301-K-FRAME) with humidity control. The illumination setup was a Celesta Light Engine solid-state laser launch (Lumencor), Celesta VCGRnIR pentaband emitter 10-10857, and Celesta VCGRnIR penta-band dichroic 10-10858. mClover3 Emission filter ET535/70m (Chroma), FM4-64 and tdTomato emission filter ET610/75m emission. The microscope was controlled through NIS-Elements software (Nikon).

Data for figures 1A and F imaging plates were prepared as described above, but before imaging a small 1.5% low-melt agarose (Sigma, A9045) pad made in K1 media was placed on top of the cells before imaging. Images were acquired using a Leica Stellaris 8 STED mounted on a Leica DMI8-CS base and using an HC PL APO CS2 86x/1.20 water objective, and Power HyD spectral detector. Images were acquired with White Light Laser (WLL) at 0.85 power percentage, taken at 1.31X zoom, 16x line averaging, 1024x1024 resolution, and mClover target wavelengths of 509.62-586.36nm and FM4-64 target wavelengths of 624.50-771.73nm. For three-dimensional reconstruction in Figure 1A, images were acquired at 1024x1024x130 with voxel size of 0.0254340084638276 x 0.0254340084638276 x 0.14839496124031007µm and visualized in ChimeraX-1.61(Goddard et al., 2018; Pettersen et al., 2021) with gaussian smoothing of nuclei and membrane (sdev 0.05).

For laser ablation of F-actin structures during cellularization (Figure 6), imaging plates of a strain expressing Lifeact-mClover3 were prepared as described for live cell imaging but with a small (2mL) pad of 10% gelatin (Fisher Scientific G7-500) made in K1 media placed on top of the center of the well just before imaging. Imaging was done in a Nikon Ti-E microscope equipped with an Andor Dragonfly spinning disk confocal fluorescence microscope equipped with 100x NA 1.45 objective (Nikon) and a built-in 1.5x magnifier; 488 nm diode laser with Borealis attachment (Andor); emission filter Chroma ET525/50m; and an EMCCD camera (iXon3, Andor Technology). Fusion software (Andor) was used to control data acquisition.

Ablations were performed using a MicroPoint (Andor) system with galvo-controlled steering to deliver 20-30 3ns pulses of 551nm light at 16-20 Hz (Andor) mounted on the Dragonfly microscope described above, as previously described (Moshtohry et al., 2022; Zareiesfandabadi and Elting, 2022). Fusion software (Andor) was used to control acquisition while IQ software (Andor) was used simultaneously to control laser ablation. At this pulse rate, the ablation process lasts ~2 s. Chroma ET610LP mounted in the dichroic position of a Nikon filter turret was used to deliver the ablation laser to the sample. Since this filter also reflects the mEGFP emission, the camera frames collected during the ablation process are blank. The behavior of the severed F-actin structures of cellularization was imaged before and immediately following

laser ablation by acquiring a single confocal plane in the 488-nm channel every second for at least one minute. The mechanism of ablative photodecomposition remains unclear but may be caused by either the propagation of a pressure wave and/or cavitation bubble dynamics (Rau et al., 2006; Venugopalan et al., 2002). The size of the damage is approximately the size of the diffraction spot of the lens <0.4 μm in the XY plane and <0.8 in the Z axis (Khodjakov et al., 1997).

Pharmacological perturbations during live-cell imaging.

About one hour before the start of the experiment (~17h), remove excess of dislodged sporangia by removing gently 2mL of the media and replacing it with 2mL of fresh prewarmed K1+Carb media, adding and removing liquid from opposite sides of the well. Repeat this wash thrice in total. To the remaining 1mL, add 1mL of 20uM FM4-64 (stock 1mg/mL in water) made in K1+Carb media for staining the plasma membrane. Bring to the microscope and place in a preheated Okolab stage top chamber (H301-K-FRAME) with humidity control (30 Celsius). Twenty individual sporangia were selected from a single well for time-lapse imaging. Imaging started at 18h, sampling every 3 or 5 min, for six hours. Pharmacological perturbations are applied by removing 1mL of media and replacing it with 2X working solution of the drug of choice. For washout experiments, 50% of the final volume of the well is replaced with fresh pre-heated media ten times. Cells were treated with 2uM final concentration of Nocodazole (Cayman Chemical; No. 13857) or equivalent volume of DMSO, 50uM of Brefeldin A (Sigma B7651) or equivalent volume of DMSO, 10uM Latrunculin B (Millipore, 428020) or equivalent volume of ethanol, 150uM p-a-blebbistatin (Cayman 22699) or equivalent volume of DMSO.

Coulter Counter cell size measurements.

1mL of zoospores from six independent culture plates of *Spizellomyces* were freshly harvested as described in the section on semi-synchronized cultures for live imaging was placed in a 25mL Accuvette (A35473; Beckman Coulter) with 24mL of freshly made 50% dilution of Isoton II diluent (C96980; Beckman Coulter) and run through a 10uM aperture tube (B42812; Beckman Coulter) on a Coulter Counter Multisizer 4e (B23005; Beckman Coulter) running on a freshly made 50% dilution of Isoton II diluent (C96980; Beckman Coulter). The Coulter counter is calibrated with 2-micron latex beads (C72513 CC; Beckman Coulter). The size distribution of zoospores and beads was exported as CSV, then processed, and visualized using JupyterLab 1.16 and R v4.1.2 facilitated by custom scripts (Kluyver et al., 2016; R Core Team, 2013).

Image processing and analyses.

To measure the angle distribution in the polyhedral tessellation of cellularization (Figure 1D), five sporangia from three independent biological replicates of control cells stained with FM4-64 and imaged during cellularization were selected. The frame before obvious signs of cellularization was selected for each sporangium and the angles between the three cleavage planes (tri-furrow) around at least ten different nodes (where furrows meet) were measured using the angle function of Fiji (Schindelin et al., 2012). As a positive control and a gauge of technical reproducibility, an artificially perfect 120-degree tri-furrow with similar proportions of thickness-length was used for generating an artificial dataset by transposition and measured the same way at the same time. The resulting dataset was processed and visualized using

JupyterLab 1.16 and R v4.1.2 facilitated by custom scripts (Kluyver et al., 2016; R Core Team, 2013).

For measuring nuclear cortical migration dynamics (Figure 2A & B) we used scikit-image (Van der Walt et al., 2014) image processing in Python with custom scripts in a Google Collab notebook. Briefly, elliptical sporangia were masked, and segmented and an ellipse was fitted to their perimeter. A second ellipse with 70% of radii from the perimeter ellipse was used as the boundary between the outer and inner 50% of the sporangial area. The nuclei were segmented via thresholding and watershed algorithms. The cortical nuclear ratio is the number of nuclei in the outer donut relative to the inner disk for each frame in the time-lapse video. The resulting measures were then processed and visualized using JupyterLab 1.16 and R v4.1.2 facilitated by custom scripts (Kluyver et al., 2016; R Core Team, 2013).

To measure the defect in patterning observed after Nocodazole treatment in cellularizing sporangia (Figure 4A & B), an ellipse was masked and fitted to circular sporangia as described above using scikit-image (Van der Walt et al., 2014) image processing in Python with custom scripts in a Google Collab notebook. Briefly, since the cleavage furrows of the outer layer of daughter cells are perpendicular to the perimeter cell wall, and thus size estimates are likely to be more accurate, a concentric ellipse at 0.85% of the fitted perimeter ellipse was drawn. The peak-to-peak distance along the profile of the FM4-64 fluorescence intensity along the perimeter of this ellipse was used as a proxy for daughter cell diameter. The resulting measures were then processed and visualized using JupyterLab 1.16 and R v4.1.2 facilitated by custom scripts (Kluyver et al., 2016; R Core Team, 2013). The statistical significance test was a one-tailed permutation test of the difference of means.

The effects of Brefeldin A on cellularization were visualized by similar sporangial segmentation and masking followed by log-polar transform using sci-kit-image (Van der Walt et al., 2014) image processing in Python with custom scripts in a Google Collab notebook. The phenotyping of the sporangia (success, Failure to Start, Network Collapse) was done by hand in Fiji (Schindelin et al., 2012). The resulting measures were then processed and visualized using JupyterLab 1.16 and R v4.1.2 facilitated by custom scripts (Kluyver et al., 2016; R Core Team, 2013).

To measure the effects of Latrunculin B on the F-actin structures during cellularization, sporangia of circular shape that did not move excessively during the experiment were selected and imported to CellProfiler 4.2.1 (McQuin et al., 2018) for segmentation. As a proxy of the level of cellularization in the actin structures, we used Haralick measures of texture (Haralick et al., 1973), the Angular Second Moment relative to the time-point right before LatB treatment—relative homogeneity—was used for visualization. The phenotyping of the effects of p-a-Blebbistatin on cellularization (completion or failure) was done by hand in Fiji (Schindelin et al., 2012).

For Particle Image Velocimetry (PIV) analyses, selected sporangia were masked in Fiji (Schindelin et al., 2012) and analyzed with OpenPIV-0.25.0 (Liberzon et al., 2021) through custom Python scripts in a Google Collab Notebook. Vector field plots (Figure 6B) and plots from the top 10% velocity vectors per PIV timepoint (Figure 6C) were generated in JupyterLab 1.16 and R v4.1.2 facilitated by custom scripts (Kluyver et al., 2016; R Core Team, 2013). Kymographs from Figure 6A were generated using Fiji (Schindelin et al., 2012) from regions 20-pixel wide centered and parallel to the ablated furrow. Recoil displacement analyses from laser ablation of late-stage polyhedra were performed via sci-kit-image (Van der Walt et al., 2014) image processing in Python with custom scripts in a Google Collab notebook. Briefly, a

10-pixel wide region centered in a line along the ablated furrow was used to measure the mean fluorescence intensity profile along the furrow. Intensity peaks were detected and used to locate and measure the inter-peak distance between the receding tips of the ablated furrow. The results were visualized using JupyterLab 1.16 and R v4.1.2 facilitated by custom scripts (Kluyver et al., 2016; R Core Team, 2013).

REFERENCES

Agarwal, P., Zaidel-Bar, R., 2019. Principles of Actomyosin Regulation In Vivo. Trends Cell Biol. 29, 150–163. https://doi.org/10.1016/j.tcb.2018.09.006

Baker, J., Theurkauf, W., Schubiger, G., 1993. Dynamic changes in microtubule configuration correlate with nuclear migration in the preblastoderm *Drosophila* embryo. J. Cell Biol. 122, 113–121. https://doi.org/10.1083/jcb.122.1.113

Barron, J.L., Hill, E.P., 1974. Ultrastructure of Zoosporogenesis in *Allomyces macrogynus*. J. Gen. Microbiol. 80, 319–327. https://doi.org/10.1099/00221287-80-2-319

Boisvieux-Ulrich, E., Lainé, M.C., Sandoz, D., 1990. Cytochalasin D inhibits basal body migration and ciliary elongation in quail oviduct epithelium. Cell Tissue Res. 259, 443–454. https://doi.org/10.1007/BF01740770

Boisvieux-Ulrich, E., Lainé, M.C., Sandoz, D., 1989. *In vitro* effects of colchicine and nocodazole on ciliogenesis in quail oviduct. Biol. Cell 67, 67–79. https://doi.org/10.1111/j.1768-322x.1989.tb03011.x

Boisvieux-Ulrich, E., Laine, M.C., Sandoz, D., 1987. I*n vitro* effects of benzodiazepines on ciliogenesis in the quail oviduct. Cell Motil. Cytoskeleton 8, 333–344. https://doi.org/10.1002/cm.970080406

Burgess, D.R., Chang, F., 2005. Site selection for the cleavage furrow at cytokinesis. Trends Cell Biol. 15, 156–162. https://doi.org/10.1016/j.tcb.2005.01.006

Coué, M., Brenner, S.L., Spector, I., Korn, E.D., 1987. Inhibition of actin polymerization by latrunculin A. FEBS Lett. 213, 316–318. https://doi.org/10.1016/0014-5793(87)81513-2

Curran, K.A., Morse, N.J., Markham, K.A., Wagman, A.M., Gupta, A., Alper, H.S., 2015. Short Synthetic Terminators for Improved Heterologous Gene Expression in Yeast. ACS Synth. Biol. 4, 824–832. https://doi.org/10.1021/sb5003357

Daga, R.R., Chang, F., 2005. Dynamic positioning of the fission yeast cell division plane. Proc. Natl. Acad. Sci. U. S. A. 102, 8228–8232. https://doi.org/10.1073/pnas.0409021102

Delsaulx, J., 1884. Les travaux scientifiques de Joseph Plateau. A. Vromant.

Deshpande, O., de-Carvalho, J., Vieira, D.V., Telley, I.A., 2022. Astral microtubule cross-linking safeguards uniform nuclear distribution in the *Drosophila* syncytium. J. Cell Biol. 221, e202007209. https://doi.org/10.1083/jcb.202007209

Deshpande, O., Telley, I.A., 2021. Nuclear positioning during development: Pushing, pulling and

flowing. Semin. Cell Dev. Biol. 120, 10–21. https://doi.org/10.1016/j.semcdb.2021.09.020

Dudin, O., Ondracka, A., Grau-Bové, X., Haraldsen, A.A., Toyoda, A., Suga, H., Bråte, J., Ruiz-Trillo, I., 2019. A unicellular relative of animals generates a layer of polarized cells by actomyosin-dependent cellularization. eLife 8, e49801. https://doi.org/10.7554/eLife.49801

Fujiwara, I., Zweifel, M.E., Courtemanche, N., Pollard, T.D., 2018. Latrunculin A Accelerates Actin Filament Depolymerization in Addition to Sequestering Actin Monomers. Curr. Biol. CB 28, 3183-3192.e2. https://doi.org/10.1016/j.cub.2018.07.082

Glotzer, M., 2017. Cytokinesis in Metazoa and Fungi. Cold Spring Harb. Perspect. Biol. 9, a022343. https://doi.org/10.1101/cshperspect.a022343

Goddard, T.D., Huang, C.C., Meng, E.C., Pettersen, E.F., Couch, G.S., Morris, J.H., Ferrin, T.E., 2018. UCSF ChimeraX: Meeting modern challenges in visualization and analysis. Protein Sci. Publ. Protein Soc. 27, 14–25. https://doi.org/10.1002/pro.3235

Goodman, E.M., Rusch, H.P., 1970. Ultrastructural changes during spherule formation in *Physarum polycephalum*. J. Ultrastruct. Res. 30, 172–183. https://doi.org/10.1016/s0022-5320(70)90071-7

Hannaford, M.R., Rusan, N.M., 2024. Positioning centrioles and centrosomes. J. Cell Biol. 223, e202311140. https://doi.org/10.1083/jcb.202311140

Haralick, R.M., Shanmugam, K., Dinstein, I.H., 1973. Textural features for image classification. IEEE Trans. Syst. Man Cybern. 610–621.

Harvey, E.B., 1935. The mitotic figure and cleavage plane in the egg of *Parechinus microtuberculatus*, as influenced by centrifugal force. Biol. Bull. 69, 287–297.

Hayashi, T., Carthew, R.W., 2004. Surface mechanics mediate pattern formation in the developing retina. Nature 431, 647–652. https://doi.org/10.1038/nature02952

Heer, N.C., Martin, A.C., 2017. Tension, contraction and tissue morphogenesis. Development 144, 4249–4260. https://doi.org/10.1242/dev.151282

Heissler, S.M., Sellers, J.R., 2015. Four things to know about myosin light chains as reporters for non-muscle myosin-2 dynamics in live cells. Cytoskelet. Hoboken NJ 72, 65–70. https://doi.org/10.1002/cm.21212

Kang, S., Tice, A.K., Spiegel, F.W., Silberman, J.D., Pánek, T., Cepicka, I., Kostka, M., Kosakyan, A., Alcântara, D.M.C., Roger, A.J., Shadwick, L.L., Smirnov, A., Kudryavtsev, A., Lahr, D.J.G., Brown, M.W., 2017. Between a Pod and a Hard Test: The Deep Evolution of Amoebae. Mol. Biol. Evol. 34, 2258–2270. https://doi.org/10.1093/molbev/msx162

Kassianidou, E., Brand, C.A., Schwarz, U.S., Kumar, S., 2017. Geometry and network connectivity govern the mechanics of stress fibers. Proc. Natl. Acad. Sci. U. S. A. 114, 2622–2627. https://doi.org/10.1073/pnas.1606649114

Khodjakov, A., Cole, R.W., Rieder, C.L., 1997. A synergy of technologies: combining laser microsurgery with green fluorescent protein tagging. Cell Motil. Cytoskeleton 38, 311–317. https://doi.org/10.1002/(SICI)1097-0169(1997)38:4<311::AID-CM1>3.0.CO;2-6

Kluyver, T., Ragan-Kelley, B., Pérez, F., Granger, B., Bussonnier, M., Frederic, J., Kelley, K., Hamrick, J., Grout, J., Corlay, S., 2016. Jupyter Notebooks–a publishing format for reproducible computational workflows, in: Positioning and Power in Academic Publishing: Players, Agents and Agendas. IOS press, pp. 87–90.

Kumar, S., Maxwell, I.Z., Heisterkamp, A., Polte, T.R., Lele, T.P., Salanga, M., Mazur, E., Ingber, D.E., 2006. Viscoelastic retraction of single living stress fibers and its impact on cell shape, cytoskeletal organization, and extracellular matrix mechanics. Biophys. J. 90, 3762–3773. https://doi.org/10.1529/biophysj.105.071506

Lecuit, T., Lenne, P.-F., 2007. Cell surface mechanics and the control of cell shape, tissue patterns and morphogenesis. Nat. Rev. Mol. Cell Biol. 8, 633–644. https://doi.org/10.1038/nrm2222

Leidel, S., Delattre, M., Cerutti, L., Baumer, K., Gönczy, P., 2005. SAS-6 defines a protein family required for centrosome duplication in *C. elegans* and in human cells. Nat. Cell Biol. 7, 115–125. https://doi.org/10.1038/ncb1220

Lessie, P.E., Lovett, J.S., 1968. Ultrastructural changes during sporangium formation and zoospore differentiation in *Blastocladiella emersonii*. Am. J. Bot. 55, 220–236.

Liberzon, A., Käufer, T., Bauer, A., Vennemann, P., Zimmer, E., 2021. OpenPIV/openpiv-python: OpenPIV-Python v0.23.4. https://doi.org/10.5281/zenodo.4409178

Lowry, D.S., Roberson, R.W., 1997. Microtubule organization during zoosporogenesis in *Allomyces macrogynus*. Protoplasma 196, 45–54. https://doi.org/10.1007/BF01281057

McQuin, C., Goodman, A., Chernyshev, V., Kamentsky, L., Cimini, B.A., Karhohs, K.W., Doan, M., Ding, L., Rafelski, S.M., Thirstrup, D., 2018. CellProfiler 3.0: Next-generation image processing for biology. PLoS Biol. 16, e2005970.

Medina, E.M., Robinson, K.A., Bellingham-Johnstun, K., Ianiri, G., Laplante, C., Fritz-Laylin, L.K., Buchler, N.E., 2020. Genetic transformation of *Spizellomyces punctatus*, a resource for studying chytrid biology and evolutionary cell biology. eLife 9, e52741. https://doi.org/10.7554/eLife.52741

Minestrini, G., Harley, A.S., Glover, D.M., 2003. Localization of Pavarotti-KLP in living *Drosophila* embryos suggests roles in reorganizing the cortical cytoskeleton during the mitotic cycle. Mol. Biol. Cell 14, 4028–4038. https://doi.org/10.1091/mbc.e03-04-0214

Moshtohry, M., Bellingham-Johnstun, K., Elting, M.W., Laplante, C., 2022. Laser ablation reveals the impact of Cdc15p on the stiffness of the contractile ring. Mol. Biol. Cell 33, br9. https://doi.org/10.1091/mbc.E21-10-0515

Okamura, S., Hayashi, K., Nishi, A., 1983. Participation of actin filaments in the plasmodial cleavage of spherulating *Physarum polycephalum*. J. Gen. Appl. Microbiol. 29, 73–77. https://doi.org/10.2323/jgam.29.73

Padilla, J.R., Ferreira, L.M., Folker, E.S., 2022. Nuclear movement in multinucleated cells. Dev. Camb. Engl. 149, dev200749. https://doi.org/10.1242/dev.200749

Pettersen, E.F., Goddard, T.D., Huang, C.C., Meng, E.C., Couch, G.S., Croll, T.I., Morris, J.H., Ferrin, T.E., 2021. UCSF ChimeraX: Structure visualization for researchers, educators, and developers. Protein Sci. Publ. Protein Soc. 30, 70–82. https://doi.org/10.1002/pro.3943

Plateau, J.A.F., 1873. Statique expérimentale et théorique des liquides soumis aux seules forces moléculaires: Tome premier. Gauthier-Villars.

Pollard, T.D., O'Shaughnessy, B., 2019. Molecular Mechanism of Cytokinesis. Annu. Rev. Biochem. 88, 661–689. https://doi.org/10.1146/annurev-biochem-062917-012530

Prostak, S.M., Medina, E.M., Kalinka, E., Fritz-Laylin, L.K., 2023. A guide to *Agrobacterium*-mediated transformation of the chytrid fungus *Spizellomyces punctatus*. Access Microbiol. 5, acmi000566.v3. https://doi.org/10.1099/acmi.0.000566.v3

R Core Team, 2013. R: A language and environment for statistical computing. Found. Stat. Comput. Vienna Austria.

Rappaport, R., 1996. Cytokinesis in animal cells. Cambridge University Press.

Rappaport, R., 1986. Establishment of the mechanism of cytokinesis in animal cells. Int. Rev. Cytol. 105, 245–281. https://doi.org/10.1016/s0074-7696(08)61065-7

Rau, K.R., Quinto-Su, P.A., Hellman, A.N., Venugopalan, V., 2006. Pulsed laser microbeam-induced cell lysis: time-resolved imaging and analysis of hydrodynamic effects. Biophys. J. 91, 317–329. https://doi.org/10.1529/biophysj.105.079921

Renaud, F.L., Swift, H., 1964. The Development of Basal Bodies and Flagella in *Allomyces arbusculus*. J. Cell Biol. 23, 339–354. https://doi.org/10.1083/jcb.23.2.339

Schindelin, J., Arganda-Carreras, I., Frise, E., Kaynig, V., Longair, M., Pietzsch, T., Preibisch, S., Rueden, C., Saalfeld, S., Schmid, B., Tinevez, J.-Y., White, D.J., Hartenstein, V., Eliceiri, K., Tomancak, P., Cardona, A., 2012. Fiji: an open-source platform for biological-image analysis. Nat. Methods 9, 676–682. https://doi.org/10.1038/nmeth.2019

Silva, A.M., Osório, D.S., Pereira, A.J., Maiato, H., Pinto, I.M., Rubinstein, B., Gassmann, R., Telley, I.A., Carvalho, A.X., 2016. Robust gap repair in the contractile ring ensures timely completion of cytokinesis. J. Cell Biol. 215, 789–799. https://doi.org/10.1083/jcb.201605080

Skejo, J., Garg, S.G., Gould, S.B., Hendriksen, M., Tria, F.D.K., Bremer, N., Franjević, D., Blackstone, N.W., Martin, W.F., 2021. Evidence for a Syncytial Origin of Eukaryotes from Ancestral State Reconstruction. Genome Biol. Evol. 13, evab096. https://doi.org/10.1093/gbe/evab096

Sokac, A.M., Biel, N., De Renzis, S., 2023. Membrane-actin interactions in morphogenesis: Lessons learned from *Drosophila* cellularization. Semin. Cell Dev. Biol. 133, 107–122.

https://doi.org/10.1016/j.semcdb.2022.03.028

Sommi, P., Ananthakrishnan, R., Cheerambathur, D.K., Kwon, M., Morales-Mulia, S., Brust-Mascher, I., Mogilner, A., 2010. A mitotic kinesin-6, Pav-KLP, mediates interdependent cortical reorganization and spindle dynamics in *Drosophila* embryos. J. Cell Sci. 123, 1862–1872. https://doi.org/10.1242/jcs.064048

Spira, F., Cuylen-Haering, S., Mehta, S., Samwer, M., Reversat, A., Verma, A., Oldenbourg, R., Sixt, M., Gerlich, D.W., 2017. Cytokinesis in vertebrate cells initiates by contraction of an equatorial actomyosin network composed of randomly oriented filaments. eLife 6, e30867. https://doi.org/10.7554/eLife.30867

Suga, H., Ruiz-Trillo, I., 2013. Development of ichthyosporeans sheds light on the origin of metazoan multicellularity. Dev. Biol. 377, 284–292. https://doi.org/10.1016/j.ydbio.2013.01.009

Tanos, B.E., Yang, H.-J., Soni, R., Wang, W.-J., Macaluso, F.P., Asara, J.M., Tsou, M.-F.B., 2013. Centriole distal appendages promote membrane docking, leading to cilia initiation. Genes Dev. 27, 163–168. https://doi.org/10.1101/gad.207043.112

Thompson, D.W., 1992. On Growth and Form, 1st ed. Cambridge University Press. https://doi.org/10.1017/CBO9781107325852

Thompson, W., 1887. On the division of space with minimal partitional area. Philos. Mag. 24, 503.

Van der Walt, S., Schönberger, J.L., Nunez-Iglesias, J., Boulogne, F., Warner, J.D., Yager, N., Gouillart, E., Yu, T., 2014. scikit-image: image processing in Python. PeerJ 2, e453.

Venugopalan, V., Guerra, A., Nahen, K., Vogel, A., 2002. Role of laser-induced plasma formation in pulsed cellular microsurgery and micromanipulation. Phys. Rev. Lett. 88, 078103. https://doi.org/10.1103/PhysRevLett.88.078103

Wollrab, V., Thiagarajan, R., Wald, A., Kruse, K., Riveline, D., 2016. Still and rotating myosin clusters determine cytokinetic ring constriction. Nat. Commun. 7, 11860. https://doi.org/10.1038/ncomms11860

Xiang, X., 2018. Nuclear movement in fungi. Semin. Cell Dev. Biol. 82, 3–16. https://doi.org/10.1016/j.semcdb.2017.10.024

Zareiesfandabadi, P., Elting, M.W., 2022. Force by minus-end motors Dhc1 and Klp2 collapses the *S. pombe* spindle after laser ablation. Biophys. J. 121, 263–276. https://doi.org/10.1016/j.bpj.2021.12.019

Zhao, H., Khan, Z., Westlake, C.J., 2023. Ciliogenesis membrane dynamics and organization. Semin. Cell Dev. Biol. 133, 20–31. https://doi.org/10.1016/j.semcdb.2022.03.021

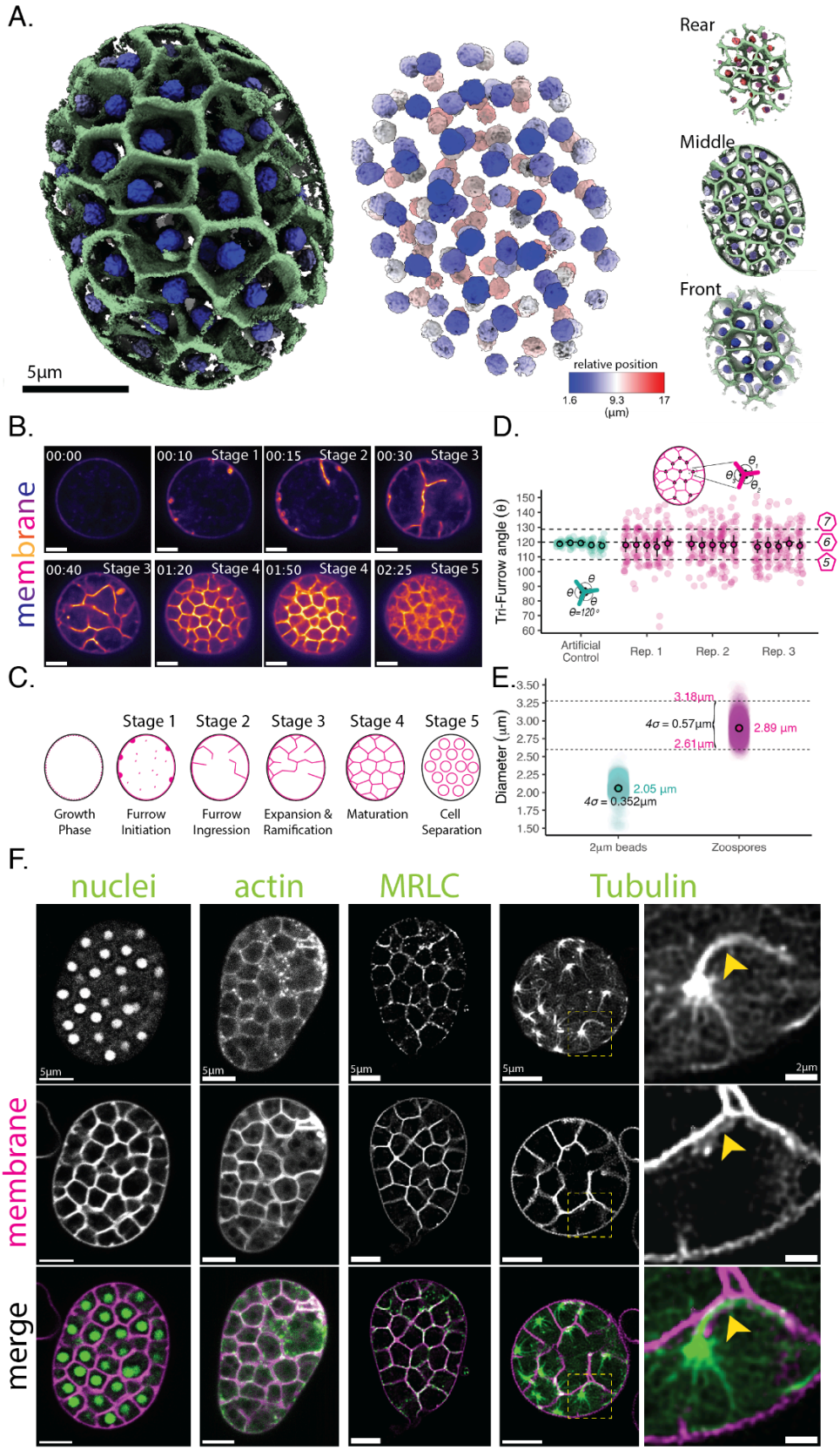
A.
5µm
relative position
1.6
9.3
17
(µm)
Rear
Middle
Front
B.
membrane
00:00
00:10
Stage 1
00:15
Stage 2
00:30
Stage 3
00:40
Stage 3
01:20
Stage 4
01:50
Stage 4
02:25
Stage 5
C.
Stage 1
Stage 2
Stage 3
Stage 4
Stage 5
Growth Phase
Furrow Initiation
Furrow Ingression
Expansion & Ramification
Maturation
Cell Separation
D.
Tri-Furrow angle (θ)
θ=120°
Artificial Control
Rep. 1
Rep. 2
Rep. 3
7
6
5
E.
Diameter (µm)
3.18µm
4σ = 0.57µm
2.89 µm
2.61µm
2.05 µm
4σ = 0.352µm
2µm beads
Zoospores
F.
nuclei
actin
MRLC
Tubulin
membrane
merge
5µm
2µm

Figure 1. The chytrid *Spizellomyces* cellularizes by building a 3D tessellation of membrane polyhedra of homogeneous size, hexagonal symmetry and demarcated by actin and myosin-II activity. (A) ChimeraX 3D reconstruction from a point scanner confocal live-cell image of a chytrid sporangium at peak cellularization. Membrane polyhedra are uninucleated and homogeneously distributed across the volume of the sporangium (front, middle, rear). FM-64 dye was used for membrane (green) and nuclear-localized mClover3 for highlighting nuclei (blue to red). The nuclear position is shown as relative depth from the first stack image. **(B & C)** Images and schematic of the five main stages of development of the membrane cleavage structures of chytrid cellularization as visualized with FM4-64. **(D)** The cellularization polyhedra have internal vertices with angles in agreement with hexagonal symmetry (magenta). The angles were measured for at least twenty vertices within the central slice of a sporangium and for five sporangia in three biological replicates. These angles were compared to a set of five artificial vertices (teal) with perfect hexagonal symmetry (120 degrees) and similar cleavage membrane thickness and proportions to assess technical measurement error. **(E)** Chytrid cellularization is very precise in the production of daughter cells of similar size. Distribution of sizes of artificial latex beads of 2µm (teal) compared to chytrid zoospores (magenta). 95% of zoospores are within 0.57µm of the mean (2.89µm). $N_{zoospores}$ = 3785, N_{beads}= 7272. Measurements made with a Coulter counter. **(F)** Actin and myosin-II colocalize with the membrane of the cellularization polyhedra. Live-cell confocal imaging of strains expressing the (nuclei) NLS-mClover3 to track nuclei (same image used in 3D reconstruction in A), the F-actin probe Lifeact-mClover3 (actin), the myosin-II probe MRLC-mClover3 (MRLC), and mClover3-α-Tubulin (Tubulin) to track microtubules. The magnified region of microtubules highlights the ciliary axoneme (yellow arrow) that starts elongating after entry into cellularization. Membrane dyed with FM4-64. Scale 5µm.

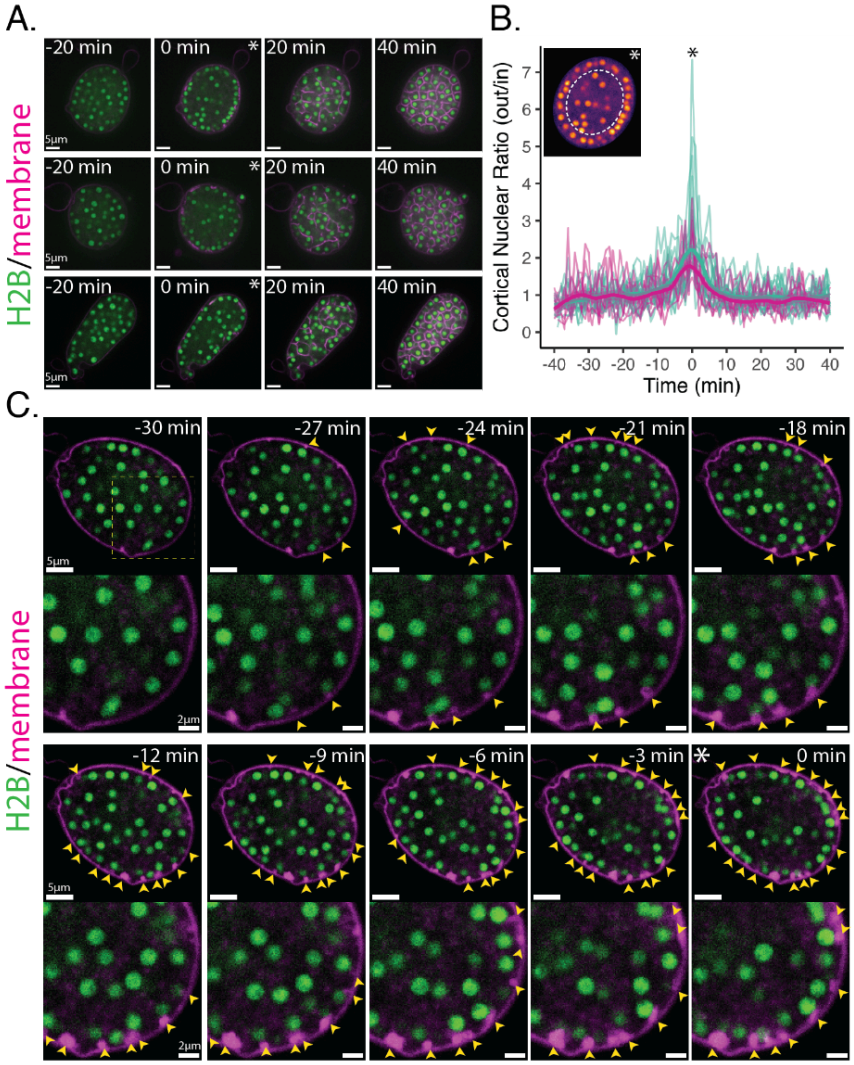

Figure 2. The onset of chytrid cellularization is marked by the recruitment of nuclei to the plasma membrane and the formation of vesicular membrane structures near cortical nuclei. (A) Chytrid nuclei (H2B-tdTomato) are homogenously distributed across the sporangium before (-20 min) and after (+20 min) entry into cellularization except for a narrow window just at entry into cellularization (0 min; asterisk; coincides with the formation of the first membrane vesicles; Stage 1) when nuclei are enriched at the plasma membrane. **(B)** Nuclear enrichment at the plasma membrane is limited to a narrow window of time (~10 min) at the onset of cellularization. After, the nuclei return to be homogeneously distributed. Quantification of nuclear dynamics during time-lapse microscopy 40 min before and after entry into cellularization. The cortical nuclear ratio (CNR) corresponds to the ratio of the number of nuclei in the outer 50% area (a donut) relative to the inner 50% area (disk)—see inset image. The CNR distribution during time-lapse imaging for each sporangium was centered on zero based on the peak cortical nuclear ratio—marked with an asterisk. **(C)** Recruitment of nuclei to the plasma membrane during entry into cellularization coincides with the formation of membrane vesicular structures (yellow arrows) in the proximity of each nucleus. Progression of nuclear recruitment and concomitant vesicular furrow initiation shown until peak cortical migration (asterisk; 0 min).

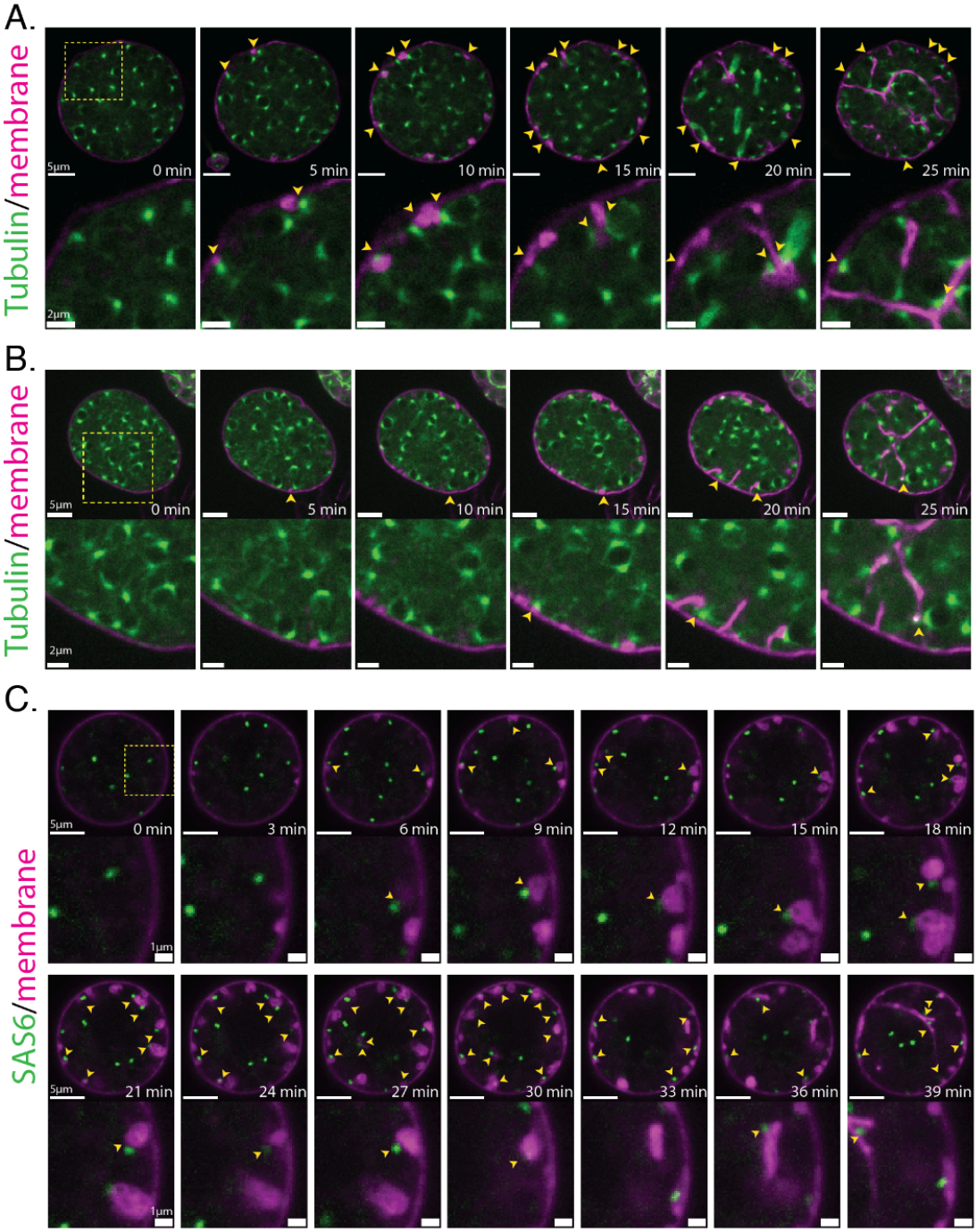

Figure 3. Cortical nuclei attach to the membrane vesicular furrow initials via the centrosomal region and are then dragged inwards when the vesicular furrows are elongated. (A & B) membrane vesicular furrows form in the proximity of the nuclear centrosomal regions (yellow arrows; 5-to-15min). The nuclei remain tethered to the membrane via the centrosomal region when the vesicular furrows extend inwards (15-to-25 min). Note that in (A) a nucleus forms a spindle and remains attached via the polar region of the spindle to the extending furrow. **(C)** A strain expressing a fluorescently tagged centrosomal component SAS6-mClover3 shows that the centrioles are proximal to the vesicular furrow initials (yellow arrows) and remain attached to the furrows during elongation. Membrane dyed with FM4-64.

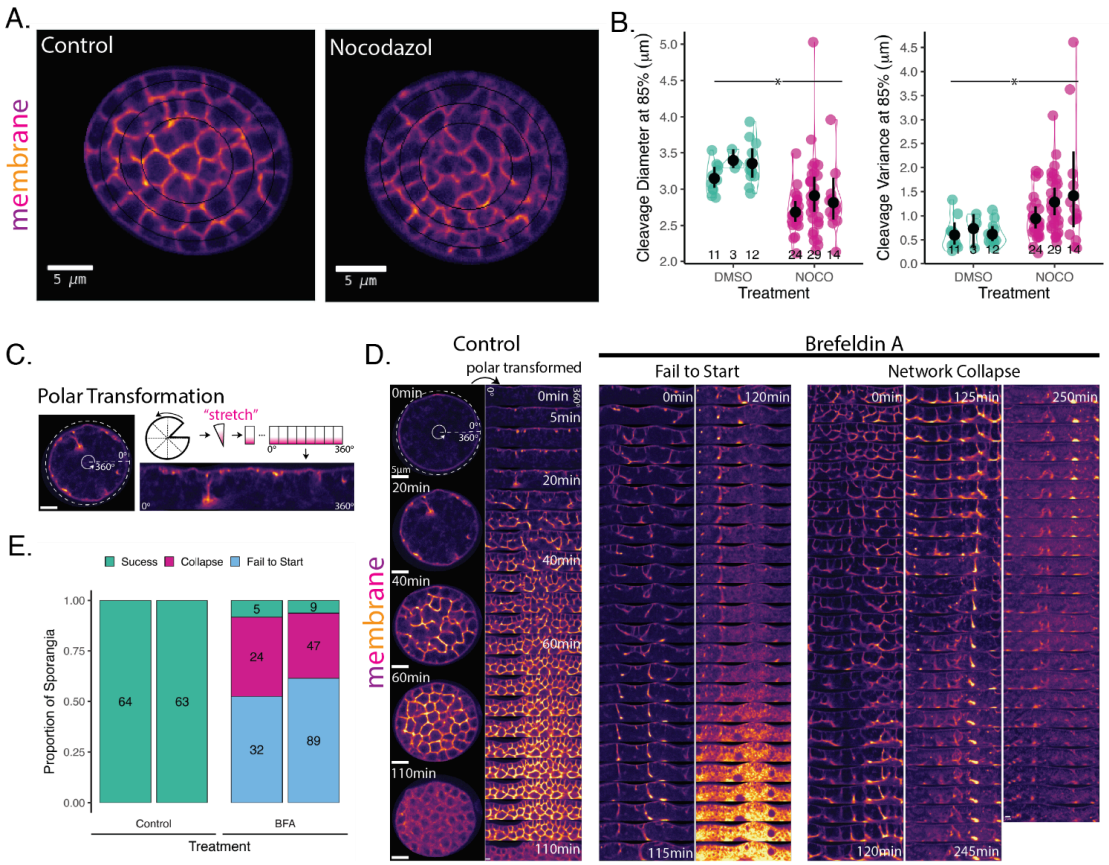

Figure 4. Depolymerization of microtubules does not inhibit cellularization but causes patterning defects and the membrane of cellularization is sourced primarily from the Golgi. (A) Sporangia treated with Nocodazole (2μM) during cellularization causes a defect in the geometric patterning of cellularization but does not inhibit it. Concentric ellipses of 85%, 65%, and 45% radii are shown in thin black lines **(B)** Daughter cells of sporangia treated with Nocodazole are smaller and are more variable in diameter than sporangia treated with the carrier control DMSO. The daughter size was estimated using the distance between max-intensity peaks in a line scan of the fluorescence intensity of the membrane along the 85% radii ellipse. Cleavage planes at 85% tend to be perpendicular to the ellipse and thus more accurate. Significance was assessed by a permutation test of the difference of means. * p-value ≤ 0.05. **(C)** Schematic of the polar transformation on an image of membrane organization (FM4-64) in a sporangium during cellularization. This transformation converts "circular" images with polar coordinates into "unwrapped" images in cartesian coordinates for easier visualization. In our case, the plasma membrane will be at the top and the furrows invade inwards towards the bottom. **(D)** Sporangia treated during cellularization with the inhibitor of ER-to-Golgi trafficking Brefeldin-A fail to complete cellularization because they either fail to start—furrows try to invade but fail to progress (left)—or cause collapse of the furrows already formed at the moment of treatment (right). In contrast, control sporangia treated with the carrier DMSO show a gradual increase in the complexity of patterning until completing cell separation (110 min). Bright FM4-64 fluorescence in the "fail to start" panel corresponds to cell death. **(E)** Quantification of the proportion of cells succeeding, failing to start, or collapsing during treatment with BFA or DMSO control.

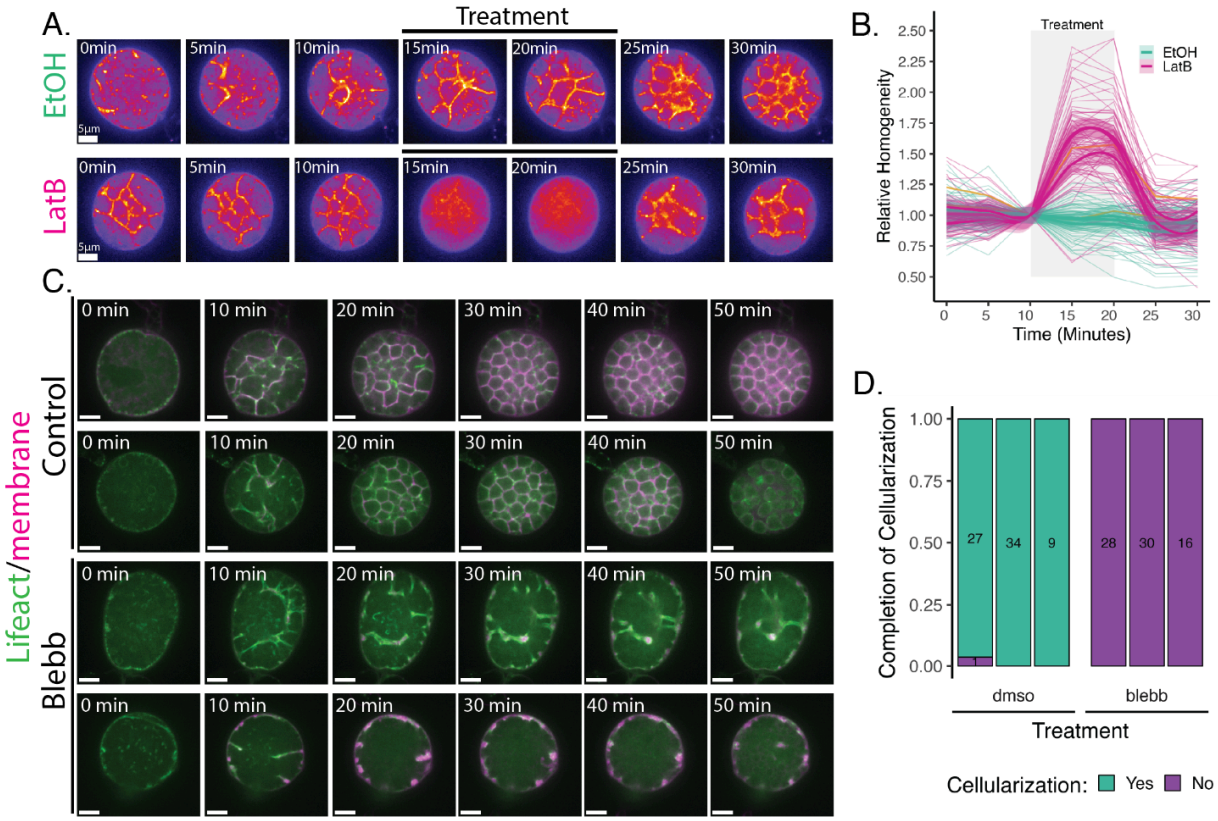

Figure 5. Chytrid cellularization requires actin polymerization and myosin-II activity. (A) Inhibition of actin polymerization with Latrunculin B (LatB) causes disassembly of the actin cellularization network. This network is reassembled within 5 min after the washout of LatB. **(B)** Treatment with LatB (magenta) causes a sharp increase in sporangial homogeneity—reduction in texture, and thus disassembly of the actin network—that comes back to pre-treatment levels after the washout of LatB. Control sporangia (teal) treated with DMSO control shows no effect. The mean line and bootstrapping 95% confidence interval of the mean are shown for three biological replicates. Orange lines show the series shown in panel (A). **(C)** Treatment of sporangia with the inhibitor of myosin-II activity para-amino-blebbistatin (Blebb) inhibits cellularization. Control cells treated with DMSO control show normal cellularization, while sporangia treated with Blebb fail to advance beyond Stage 1 or 2. **(D)** Treatment of sporangia with Blebb completely inhibits cellularization. The box for each of the three biological replicates shows the number of sporangia analyzed per replicate.

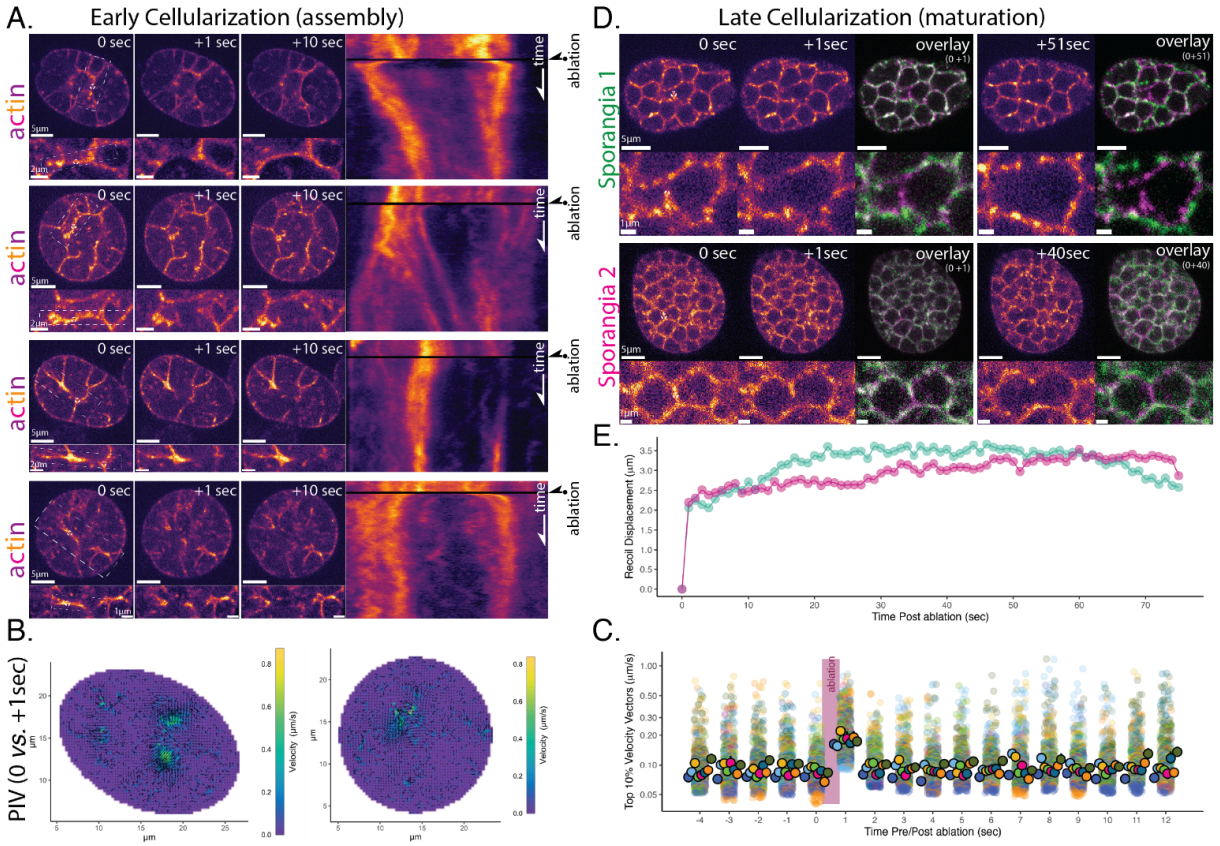

Figure 6. The actomyosin furrows of early cellularization and the edges of the late cellularization polyhedra are under tension. (A) Laser ablation of the actin furrows of early cellularization results in recoil, suggesting that these structures are under tension and are likely contractile. Four examples of sporangia are shown. Still images of the sporangia just before laser ablation (0 sec) and then 1 and 10 seconds after laser ablation. The site of ablation is shown with a white dashed dot. The magnified inset image shown below is demarcated with a dashed white region in the top image. The selected region in the inset image is the 20-pixel width selection used for the kymograph on the right. Each row represents the sum of intensities of the 20-pixel region before and after laser ablation. Note the fast recoil response after the dark row (laser ablation) and the tendency of the actin structure to contract and "repair" the structures in the damaged region. **(B)** To quantify changes in the speed and direction of all actin structures of cellularization after ablation, we used particle image velocimetry. We show two examples of changes in the direction and speed of the actin between the frame just before laser ablation (0 sec) and after ablation (1 sec) for the top two examples in panel (A). Note vectors with high velocity (warm color) moving away from the ablation site (recoil). **(D)** Quantification of the top 10% high-velocity vectors for each frame before and after laser ablation for eight different sporangia (different colors). Note the sharp increase in velocity right after ablation in agreement with a recoil response. **(D)** Laser ablation of the membrane polyhedra of late cellularization also results in recoil and dilation of the polyhedral geometry. Overlay for frames before and right after ablation and near maximal recoil displacement. **(E)** Recoil displacement caused by ablation of the sporangia shown in D (pink and green). The recoil of the polyhedral edges shows a sharp fast recoil of about ~2µm—severed furrow—followed by slower dilation of the surrounding polyhedra. Quantification of recoil displacement performed by automated calculation of interpeak distances from the intensity distribution for a line 10-pixel wide along the ablated cleavage plane.

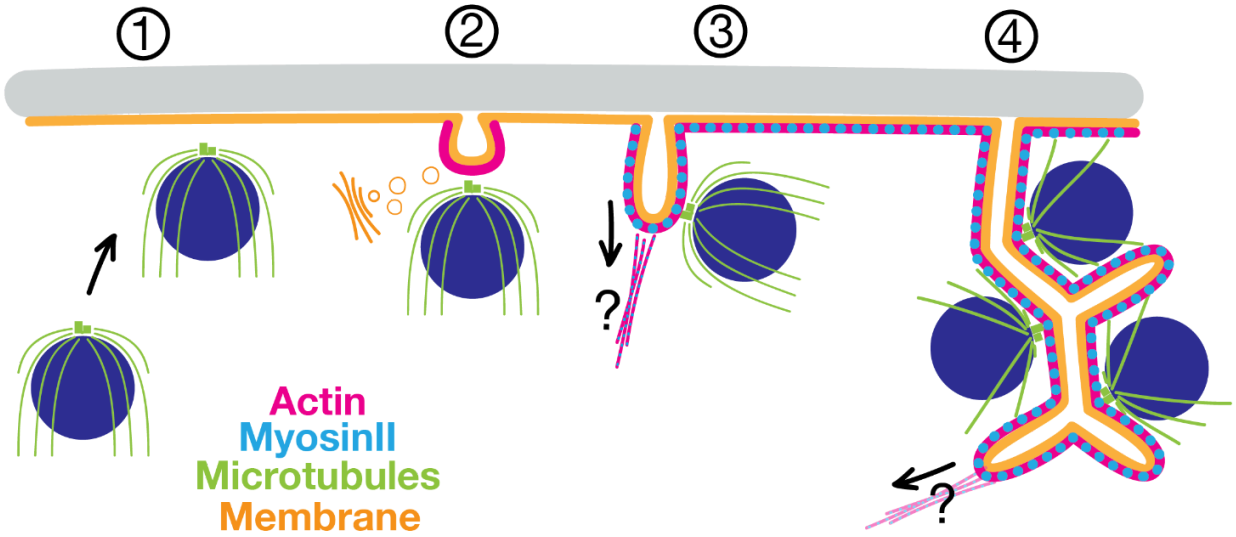

Figure 7. The model of chytrid 3D cellularization. (1) Nuclear cortical migration: Entry into cellularization is marked by the recruitment of nuclei to the plasma membrane, each nucleus with the centriolar centrosome facing toward the plasma membrane. **(2) Vesicular furrow initiation:** a vesicular membrane furrow initial is formed between the nuclear centriole and the plasma membrane. This stage does not depend on myosin-II and the membrane sourced from this stage onwards is derived from the Golgi apparatus. **(3) Furrow ingression and nuclear docking:** Actin and myosin-II drive together the extension of these vesicular furrows into tubular furrows that invade the cytoplasm. The nuclei remain attached to their furrows by the centrosomal region and are dragged inwards into the cytoplasm. Although nuclear docking may happen during furrow initiation (stage 2), we can only see it indirectly thus far due to their physical tethering during furrow ingression. **(4) Assembly of the polyhedral tessellation:** Tubular furrows branch and merge to generate the polyhedral territories of cellularization, each with a single nucleus inside. The microtubules play a role in proper nuclear distancing and geometry of the polyhedral territories. The ciliary axonemes extend in between the leaves of the double-membrane of the polyhedral faces. After a maturation time of the polyhedral tessellation, the zoospores undergo cell separation and swim or crawl out through an opening the the cell wall of the mother.

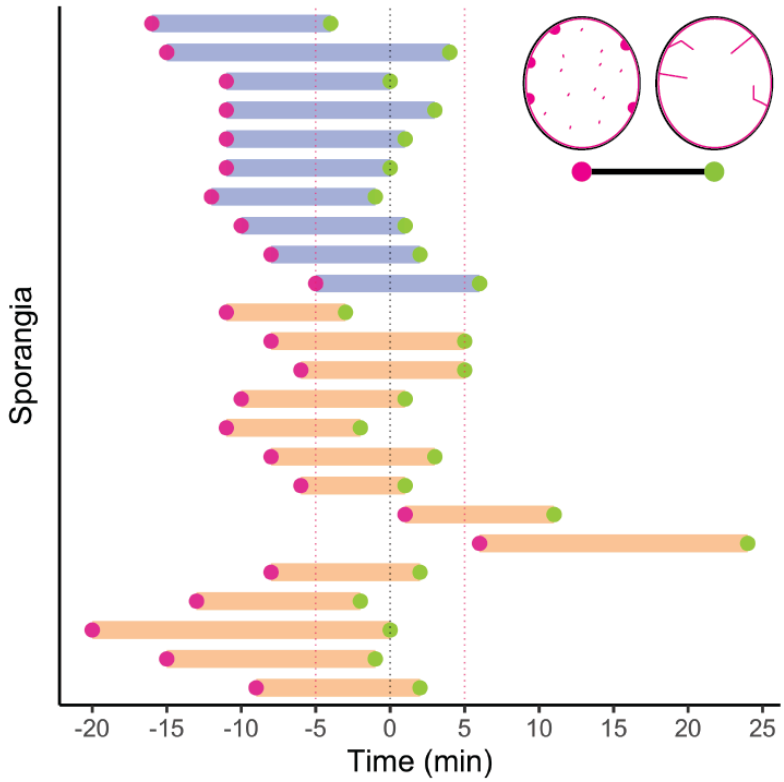

Figure S1. Furrow ingression coincides with peak cortical nuclear migration. Each sporangium (row) shows peak cortical nuclear ratio (CNR) at time 0 min. The color bar represent time relative to peak CNR from formation of the first vesicular furrow initial (magenta dot) to the moment the first furrow invades the cytoplasm (green dot). Note how most green dots are within 10 min around peak CNR. Different bar colors represent experiments from different days.

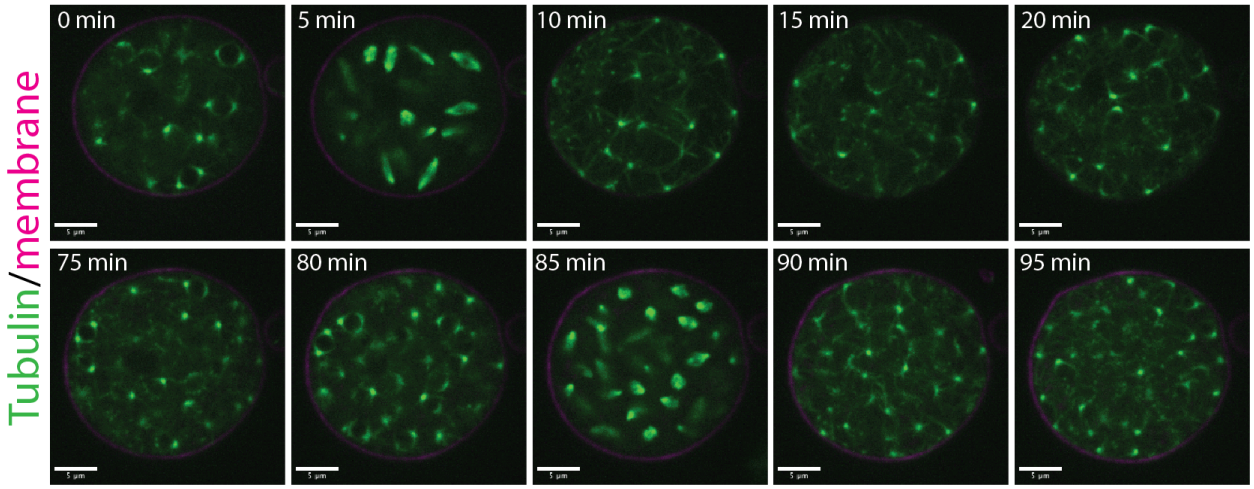

Figure S2. Nuclear-associated foci of fluorescently-tagged tubulin are likely chytrid centrosomes. Expression of fluorescently-tagged chytrid alpha-tubulin highlights centrosome-like foci at the poles of each nuclei that turn into opposing spindle poles during nuclear division. Scale bar is 5 microns.

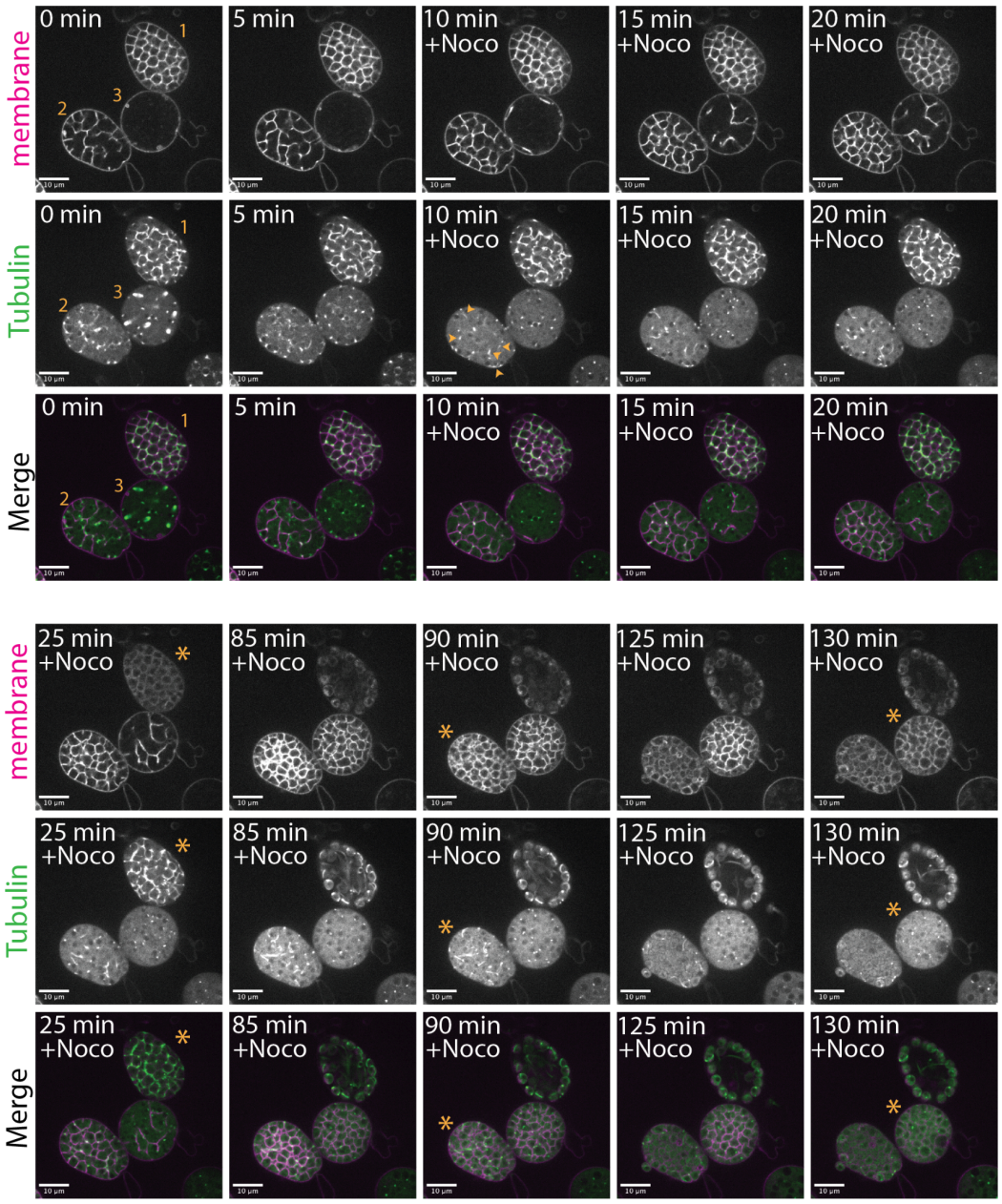

Figure S3. Cellularization in the presence of Nocodazole does not inhibit cellularization but produces defects in patterning and daughters without cilium. Example of three mother cells at different stages in cellularization during treatment with Nocodazole (10 min onwards). Note how Nocodazole causes disipation of fluorescent structures except for the bright foci at each nuclei (putative centrosome) and defects in polyhedral patterning. Mother 1 (see yellow numbers) is fully cellularized with daughters fully ciliated. This mother completes cellularization (25 min; asterisk) and daughters escape the mother's cell wall. Mother 2 is at stage 2 of cellularization (branching & merging) and shows some nuclei starting to extend their axoneme (yellow arrows; 10 min) by the time of treatment. This results in a combination of daughters with and without cilia, but still completes cellularization (90 min; asterisk). Mother 3 is at stage 1-2 of cellularization (furrow initiation). Cellularization is completed at 130 min (asterisk) and produces daughter that completely lack cilium. Scale bar 5 microns.

SUPPLEMENTARY VIDEO LEGENDS

Supplementary Video 1. F-actin colocalizes with the cellularization membrane polyehedra of a live chytrid mother cell about to reach peak cellularization. F-actin (Lifeact-mClover3) shown in green and membrane (FM4-64) in magenta. Note a small section is not completely cellularized. Laser-scanning confocal imaging. Mother cell is about 20 microns deep: Z-plane sweep of 138 Z-stacks, each 0.148 microns. Scale 5 microns.

Supplementary Video 2. Distribution of nuclei during chytrid peak cellularization. Nuclei (RbNLS-mClover3) shown in green and membrane (FM4-64) in magenta. Laser-scanning confocal imaging. Mother cell is about 20 microns deep: Z-plane sweep of 130 Z-stacks, each 0.148 microns. Scale 5 microns.

Supplementary Video 3. Distribution of myosin-II light regulatory chain (MLRC) during chytrid peak cellularization. A probe of myosin-II activity, MLRC (MLRC-mClover3) in shown in green and membrane (FM4-64) in magenta. Laser-scanning confocal imaging. Mother cell is about 20 microns deep: Z-plane sweep of 136 Z-stacks, each 0.148 microns. Scale 5 microns.

Supplementary Video 4. Microtubule architecture during chytrid peak cellularization. Chytrid alpha-tubulin (mClover3-alpha-Tubulin) in shown in green and membrane (FM4-64) in magenta. Laser-scanning confocal imaging. Z-plane sweep of 28 Z-stacks, each 0.6 microns. Scale 5 microns.

Supplementary Video 5. Nuclear dynamics during chytrid cellularization. Nuclei visualized with fluorescently-tagged histone H2B (H2B-tdTomato) are shown in green and membrane (FM4-64) in magenta. Spinning-disk confocal time-lapse. Sampling rate of one image per minute. You can see the last two nuclear divisions before the chytrid mother enters cellularization. Scale 5 microns.

Supplementary Video 6. Example of Nuclear cortical migration during chytrid cellularization. Nuclei visualized with fluorescently-tagged histone H2B (H2B-tdTomato) are shown in green and membrane (FM4-64) in magenta. Nuclei reach peak cortical ratio around 295 minutes. Spinning-disk confocal time-lapse. Sampling rate of one image per minute. You can see the last two nuclear divisions before the chytrid mother enters cellularization. Scale 5 microns.

Supplementary Video 7. Example 1 of outward-facing nuclear centrosomes during entry into cellularization. Fluorescently-tagged tubulin (mClover3-alpha-Tubulin) shown in green and membrane (FM4-64) in magenta. Note how during cortical nuclear recruitment, the nuclear-associated centrosomes are often positioned towards the plasma membrane (100-110 min). Spinning-disk confocal time-lapse. Sampling rate of one image every five minutes. Scale 5 microns.

Supplementary Video 8. Example 2 of outward-facing nuclear centrosomes during entry into cellularization. Fluorescently-tagged tubulin (mClover3-alpha-Tubulin) shown in green and membrane (FM4-64) in magenta. Mitotic spindles are visible during nuclear division (85min), and during entry into cellularization (140 min). Note how during cortical nuclear recruitment, the nuclear-associated centrosomes are often positioned towards the plasma membrane (135 min). Nuclei remain tethered to the invading furrow via the centrosome. Spinning-disk confocal

time-lapse. Sampling rate of one image every five minutes. Scale 5 microns.

Supplementary Video 9. **Example 3 of outward-facing nuclear centrosomes during entry into cellularization.** Fluorescently-tagged tubulin (mClover3-alpha-Tubulin) shown in green and membrane (FM4-64) in magenta. Note how during cortical nuclear recruitment, the nuclear-associated centrosomes are often positioned towards the plasma membrane (25 min). Nuclei remain tethered to the invading furrow via the centrosome. Spinning-disk confocal time-lapse. Spinning-disk confocal time-lapse. Sampling rate of one image every five minutes. Scale 5 microns.

Supplementary Video 10. Example 4 of microtubular dynamics during chytrid cellularization. Fluorescently-tagged tubulin (mClover3-alpha-Tubulin) shown in green and membrane (FM4-64) in magenta. Spinning-disk confocal time-lapse. Spinning-disk confocal time-lapse. Sampling rate of one image every five minutes. Scale 5 microns.

Supplementary Video 11. Chytrid centrioles appear to dock and tether to the cellularization furrows during chytrid cellularization (Example 1). Fluorescently-tagged component of the centriole SAS6 (SAS6-mClover3) shown in green and membrane (FM4-64) in magenta. Spinning-disk confocal time-lapse. Spinning-disk confocal time-lapse. Sampling rate of one image every three minutes. Scale 5 microns.

Supplementary Video 12. Chytrid centrioles appear to dock and tether to the cellularization furrows during chytrid cellularization (Example 2). Fluorescently-tagged component of the centriole SAS6 (SAS6-mClover3) shown in green and membrane (FM4-64) in magenta. Spinning-disk confocal time-lapse. Spinning-disk confocal time-lapse. Sampling rate of one image every three minutes. Scale 5 microns.

Supplementary Video 13. Chytrid mothers exposed to Brefeldin-A during late cellularization show collapse of the cellularization furrows. Fluorescently-tagged tubulin (mClover3-alpha-Tubulin) shown in green and membrane (FM4-64) in magenta. Spinning-disk confocal time-lapse. Sampling rate of one image every three minutes. Scale 5 microns.

Supplementary Video 14. Chytrid mothers exposed to Brefeldin-A before entry into cellularization fail to enter cellularization. Fluorescently-tagged tubulin (mClover3-alpha-Tubulin) shown in green and membrane (FM4-64) in magenta. Spinning-disk confocal time-lapse. Sampling rate of one image every three minutes. Scale 5 microns.

Supplementary Video 15. The actin-based furrows of early cellularization are under tension and recoil where severed by laser ablation (Example 1). Spinning-disk confocal time-lapse imaging of central plane of a strain expressing the F-actin probe Lifeact-mClover. The actin structures are severed using a laser. Note the fast recoil response after ablation. Scale 5 microns.

Supplementary Video 16. The actin-based furrows of early cellularization are under tension and recoil where severed by laser ablation (Example 2). Spinning-disk confocal time-lapse imaging of central plane of a strain expressing the F-actin probe Lifeact-mClover. The actin structures are severed using a laser. Note the fast recoil response after ablation. Scale 5 microns.

Supplementary Video 17. The actin-based furrows of early cellularization are under tension and recoil where severed by laser ablation (Example 3). Spinning-disk confocal

time-lapse imaging of central plane of a strain expressing the F-actin probe Lifeact-mClover. The actin structures are severed using a laser. Note the fast recoil response after ablation. Scale 5 microns.

Supplementary Video 18. The actin-based furrows of early cellularization are under tension and recoil where severed by laser ablation (Example 4). Spinning-disk confocal time-lapse imaging of central plane of a strain expressing the F-actin probe Lifeact-mClover. The actin structures are severed using a laser. Note the fast recoil response after ablation. Scale 5 microns.

Supplementary Video 19. The actin-based furrows of early cellularization are under tension and recoil where severed by laser ablation (Example 6). Spinning-disk confocal time-lapse imaging of central plane of a strain expressing the F-actin probe Lifeact-mClover. The actin structures are severed using a laser. Note the fast recoil response after ablation. Scale 5 microns.

Supplementary Video 20. **The actin-based furrows of early cellularization are under tension and recoil where severed by laser ablation (Example 7).** Spinning-disk confocal time-lapse imaging of central plane of a strain expressing the F-actin probe Lifeact-mClover. The actin structures are severed using a laser. Note the fast recoil response after ablation. Scale 5 microns.

Supplementary Video 21. The polyhedra of chytrid cellularization are under tension (Example 1). Spinning-disk confocal time-lapse imaging of central plane of a strain expressing the F-actin probe Lifeact-mClover. The actin structures are severed using a laser. Note the fast recoil response after ablation followed by deformation of the neighboring polyhedra. Scale 5 microns.

Supplementary Video 22. The polyhedra of chytrid cellularization are under tension (Example 2). Spinning-disk confocal time-lapse imaging of central plane of a strain expressing the F-actin probe Lifeact-mClover. The actin structures are severed using a laser. Note the fast recoil response after ablation followed by deformation of the neighboring polyhedra. Scale 5 microns.